

# A CMOS Magnetic Sensor Chip for Biomedical Applications

*Paul Liu*

Electrical Engineering and Computer Sciences  
University of California at Berkeley

Technical Report No. UCB/EECS-2012-102

<http://www.eecs.berkeley.edu/Pubs/TechRpts/2012/EECS-2012-102.html>

May 11, 2012



Copyright © 2012, by the author(s).  
All rights reserved.

Permission to make digital or hard copies of all or part of this work for personal or classroom use is granted without fee provided that copies are not made or distributed for profit or commercial advantage and that copies bear this notice and the full citation on the first page. To copy otherwise, to republish, to post on servers or to redistribute to lists, requires prior specific permission.

A CMOS Magnetic Sensor Chip for Biomedical Applications

by

Peng Liu

A dissertation submitted in partial satisfaction of the  
requirements for the degree of

Doctor of Philosophy

in

Engineering – Electrical Engineering and Computer Sciences

in the

GRADUATE DIVISION

of the

UNIVERSITY OF CALIFORNIA, BERKELEY

Committee in charge:

Professor Bernhard E. Boser, Chair

Professor Seth Sanders

Professor Yuri Suzuki

Spring 2012

The dissertation of Peng Liu, titled A CMOS Magnetic Sensor Chip for Biomedical Applications, is approved:

Chair \_\_\_\_\_

Date \_\_\_\_\_

\_\_\_\_\_

Date \_\_\_\_\_

\_\_\_\_\_

Date \_\_\_\_\_

University of California, Berkeley

**A CMOS Magnetic Sensor Chip for Biomedical Applications**

Copyright © 2012

by

Peng Liu

## Abstract

A CMOS Magnetic Sensor Chip for Biomedical Applications

by

Peng Liu

Doctor of Philosophy in  
Engineering - Electrical Engineering and Computer Sciences

University of California, Berkeley

Professor Bernhard E. Boser, Chair

The growing need for point-of-care applications in global health and personalized medicine motivates a significant reduction in the size and cost of present technologies. Current solutions use fluorescent or enzymatic labels with complex optical instrumentation that has proven difficult to miniaturize. Recently, magnetic bead labeling has emerged as an alternative solution enabling portable and low-cost platforms.

A compact and robust magnetic label detector for biomedical assays is implemented in 0.18- $\mu\text{m}$  CMOS. No external magnet, reference sensor or baseline calibration is required. Detection relies on the magnetic relaxation signature of a microbead label for improved tolerance to environmental variations and relaxed dynamic range requirement. Correlated double sampling combined with offset servo loops and magnetic field modulation, suppresses the detector offset to sub- $\mu\text{T}$ . Single 4.5- $\mu\text{m}$  magnetic beads are detected in 16 ms with a probability of error  $< 0.1\%$ . Magnetic imaging and bead differentiation based on relaxation are demonstrated which could potentially lead to new applications.

*To my family*

# Table of Contents

<b>Table of Contents .....</b>	<b>ii</b>
<b>List of Figures.....</b>	<b>iv</b>
<b>List of Tables .....</b>	<b>vii</b>
<b>Chapter 1 Introduction.....</b>	<b>1</b>
<b>Chapter 2 Magnetic Label Detection .....</b>	<b>4</b>
2.1 Magnetic Labels .....	4
2.2 Detectors .....	10
2.3 Detection Methods .....	13
2.4 Summary .....	15
<b>Chapter 3 Magnetic Relaxation.....</b>	<b>16</b>
3.1 Origin .....	16
3.2 Magnetorelaxometry .....	19
3.3 Complex Susceptibility.....	22
3.4 Summary .....	27
<b>Chapter 4 Design Challenges and Solutions.....</b>	<b>28</b>
4.1 Hall Effect.....	28
4.2 Post-processing .....	30
4.3 Design Challenges .....	32
4.4 Solutions .....	37
4.5 Summary .....	41
<b>Chapter 5 System and Circuit Design.....</b>	<b>42</b>
5.1 System Architecture.....	42
5.2 Hall-effect Sensor Element and Array .....	44
5.3 On-chip Electromagnet and Modulation.....	53
5.4 Readout Channel .....	55
5.4.1 Offset Servo Loop .....	55
5.4.2 PGA and DAC.....	58
5.5 Discussion .....	61
5.6 Chip Implementation .....	63
5.7 Summary .....	64

<b>Chapter 6 Measurement Results .....</b>	<b>65</b>
6.1 Sensor Characterization .....	65
6.2 Bead Relaxation .....	66
6.3 Single Bead Detection.....	68
6.4 Bead Imaging.....	70
6.5 Bead Differentiation.....	71
6.6 Summary .....	74
<b>Chapter 7 Conclusions and Future Work .....</b>	<b>76</b>
7.1 Conclusions.....	76
7.2 Future Work .....	77
<b>Bibliography .....</b>	<b>78</b>

## List of Figures

Figure 1-1: Comparison of conventional (optical) and emerging (magnetic) assays. (a) “Sandwich” enzyme-linked immunosorbent assays (ELISA) and (b) magnetic immunoassays (MIA).....	2
Figure 2-1: Composition of a Dynabead. Each bead consists of magnetic nanoparticles (MNPs) dispersed in a polymer matrix.....	5
Figure 2-2: Magnetization versus magnetic field at room temperature for M-280 (left) and M-450 (right) in the field range of ( $\pm 1$ T) [7]. Inset figures show the magnetization curves at low-field ( $\pm 10$ mT). .....	5
Figure 2-3: Simulated bead magnetization dependence on MNP size distribution. Four beads with the same saturation magnetic moment are simulated. Bead 1 contains two 12-nm MNPs; Bead 2 consists of sixteen 6-nm MNPs; Bead 3 consists of half of Bead 1 and Bead 2 (one 12-nm MNP and eight 6-nm MNPs) whereas Bead 4 has the same number of MNPs as Bead 3, but all MNPs are identical (7.3nm). The magnetization curves are plotted based on Eq. (2.2) and Eq. (2.3) with $M_s = 350$ kA/m and $T = 300$ K. ....	9
Figure 2-4: Cross section of a typical magnetic label detector. ....	10
Figure 2-5: Block diagrams of previous magnetic label detectors. (a) Bead Array Counter (BARC) by NRL [5] and (b) Hall-effect sensor by EPFL [9]. The three building blocks are highlighted (red: sensor; orange: magnetizing field generator; purple: readout electronics). ....	12
Figure 2-6: Conventional detection method based on bead magnetization .....	14
Figure 2-7: Detection method based on bead relaxation .....	14
Figure 3-1: Effect of the magnetizing field on MNPs. (a) Each MNP is considered a tiny magnet. When no external field is applied, the MNPs are randomly oriented. When an external field $\mathbf{H}$ is on, the magnets tend to align with $\mathbf{H}$ . (b) Magnetic moment $\mathbf{m}$ of the MNP highlighted in (a), when $\mathbf{H}$ is applied. $\gamma$ is the angle between its easy axis and $\mathbf{H}$ with a range of $[0, \pi/2]$ . ....	17
Figure 3-2: Simulated magnetic energy of a MNP with uniaxial easy axis in low magnetizing field. ....	18
Figure 3-3: Bead magnetic moment in magnetization and relaxation .....	20

Figure 3-4: Simulated magnetic relaxation of a bead model with different magnetization time. The bead contains only 8-nm and 10-nm MNPs. ....	21
Figure 3-5: Simulated complex susceptibility for the bead model discussed in Section 3.2. The bead has only 8-nm and 10-nm MNPs. ....	23
Figure 3-6: Real (top) and imaginary part (bottom) of the measured (red) and projected (black) complex susceptibility on Dynabeads M-450. The values are normalized to DC susceptibility.....	24
Figure 3-7: Parameters in bead relaxation that affect SNR and measurement time ....	26
Figure 3-8: Contour plot of FOM vs. magnetization time and sampling time .....	26
Figure 4-1: The working principle of a Hall plate. The basic physical principle underlying the Hall effect is the Lorentz force. ....	29
Figure 4-2: Post-processing steps. A) Original chip fabricated by CMOS foundry; B) ILDs removed by RIE with metal layers serving as masks; C) Metals layers removed by wet etching and sensor surface created.....	30
Figure 4-3: Cross section and working principle of a CMOS magnetic label detector	31
Figure 4-4: Bead detector model for an easy calculation of magnetizing field. The magnetizing field is generated by a pair of long wires carrying current $I_{mag}$ in opposite directions. ....	33
Figure 4-5: Calculation of the induced magnetic field from a bead to the underlying sensor. $\mathbf{m}$ is the magnetic moment of the bead which is modeled as a dipole located at the bead center and $\mathbf{r}$ is a vector pointing from bead center to the sensor.....	35
Figure 4-6: Magnetizing field modulation timing diagram .....	37
Figure 4-7: Spectrum of a sensor output after field modulation. No low-frequency non-idealities are shown here due to a high-pass RC filter (1 kHz cutoff frequency) in the measurement path. Flicker noise corner is about 50 kHz. ....	38
Figure 4-8: Suppression of DC offset and thermal effects by CDS (not to scale).....	39
Figure 4-9: Reconstruction of signal with modulation and CDS (not to scale). Top: Modulated signal is distorted by DC offset and thermal effect. Bottom: DC offset and thermal effects removed by CDS. ....	40
Figure 5-1: Block diagram of a CMOS bead relaxation detector .....	43
Figure 5-2: Induced field from a MyOne bead on a 4- $\mu\text{m}$ by 4- $\mu\text{m}$ Hall-effect sensor. Magnetizing current is 32 mA. The distance between the magnetizing wires is 6 $\mu\text{m}$ . ....	44
Figure 5-3: Sensor element schematic .....	45
Figure 5-4: Simplified Hall plate model .....	46
Figure 5-5: Layout of a sensor element. Sensing contacts are defined by N+ doping. Metal one layer runs horizontally for magnetizing, sensor bias and row selection.	

Poly-silicon is used for signal output routing. Each sensor element occupies $8.5 \mu\text{m} \times 6 \mu\text{m}$ .	47
Figure 5-6: Noise model of a sensor element	49
Figure 5-7: Sensor array schematic. Two bias switches are added in each row.	50
Figure 5-8: Sensor array layout. Sensor switches are located on two sides of the sensor array. Sensor bias lines of adjacent rows are connected to reduce voltage drop.	51
Figure 5-9: Micrograph of an 8x8 sensor array	52
Figure 5-10: On-chip electromagnet. (a) Switch network for one row of sensors and (b) timing diagram of the switches.	54
Figure 5-11: Offset and noise sources	55
Figure 5-12: Block diagram of the mixed-signal loop for offset cancellation.	56
Figure 5-13: Timing diagram of sensor offset calibration and measurement	57
Figure 5-14: Schematic diagram of one gain stage and DAC	59
Figure 5-15: Schematic diagram of the constant-gm bias circuit	60
Figure 5-16: Sensor sleep mode for power saving.	62
Figure 5-17: Die photo of the magnetic bead detector	63
Figure 6-1: Measured Dynabead relaxation signal	66
Figure 6-2: Baseline change vs. ambient temperature. The relaxation baseline variation is much smaller than single $2.8\text{-}\mu\text{m}$ bead signal (dotted lines); the magnetization baseline is fitted and its temperature coefficient is $0.33 \text{ bead}/^\circ\text{C}$ (solid line).	67
Figure 6-3: Measurement of signal-to-noise ratio	69
Figure 6-4: Magnetic vs. optical image. Left: sensor array with M-450 beads; right: corresponding electrical signal from the sensors.	70
Figure 6-5: Measured relaxation curves (solid lines) and model (dotted). The “dead zone” is shaded. (a) $t_m = t_r = 1 \mu\text{s}$ ; (b) $t_m = t_r = 4 \mu\text{s}$ ; (c) $t_m = t_r = 16 \mu\text{s}$ ; (d) $t_m = t_r = 64 \mu\text{s}$ .	72
Figure 6-6: Real (top) and imaginary part (bottom) of the measured complex susceptibility on the three MNP samples: 20-nm MNP (blue), 25-nm MNP (red) and SiMAG (black). The values are normalized to DC susceptibility.	73

## List of Tables

Table 2-1: Characterization Results of Dynabeads [8].....	6
Table 4-1: Summary of Design Challenges and Solutions .....	41
Table 6-1: Chip Performance Summary .....	75

## Acknowledgements

First and foremost I would like to express my sincere gratitude to my advisor, Professor Bernhard Boser, for his guidance and support throughout my PhD study. I am especially grateful for his patience and encouragement at times when I was facing challenges in my research. His enthusiasm for creative ideas, his dedication to research and his scientific rigor, have greatly influenced me.

I am indebted to Professor Seth Sanders and Professor Yuri Suzuki for taking the time reviewing my dissertation and giving feedback during my qualifying exam. I have benefited greatly from the courses Professor Suzuki taught at Berkeley. I am also grateful to Professor Richard White for serving on my qualifying exam committee.

My special thanks to current and former members of Boser group who have worked on the biosensor project. First I would like to thank Karl Skucha for doing all the post processing and working on the experiments. It has been a great pleasure and honor to work with Dr. Mischa Megens, Dr. Simone Gambini and Dr. Jungkyu Kim as a multidisciplinary team. I am thankful to Yida Duan for his help to meet a tight tapeout schedule and being a nice officemate. I also would like to thank Igor Izyumin for helping the test setup. I felt lucky to conduct research based on the previous works from Dr. Turgut Aytur, Dr. Octavian Florescu, Dr. Lisen Wang and Amy Wu.

I also would like to express my thanks to Professor Frances Hellman and her group for generously allowing me using their SQUID magnetometer, to Professor John Clarke for discussions on magnetic beads and to Professor Natalie Adolphi for her advice on the magnetic relaxation experiment. I gratefully acknowledge NIH for funding my PhD research.

My time at Berkeley was made enjoyable in large part due to many talented colleagues and close friends I met here, including Yu Ben, Jiashu Chen, Jun-Chau Chien, Yida Duan, Chenjie Gu, Zhaoyi Kang, Mitchell Kline, Lingkai Kong, Han-Phuc Le, Wen Li, Yue Lu, Richie Przybyla, Richard Su, Charles Wu, Lu Ye, Wenting Zhou and many others.

Last but not least, I owe my deepest gratitude to my family for their unconditional love, especially to my wife Wei – this dissertation would not have been possible without her consistent support and encouragement.

# Chapter 1

## Introduction

Point-of-care (POC) diagnostic tools are in great demand to meet the challenges in personalized medicine and global health, where sensitivity, specificity, portability, affordability and quantitative readout with minimum laboratory infrastructure are required [1].

Optical diagnostic methods have been widely used in biomedical applications such as enzyme-linked immunosorbent assays (ELISA) (Figure 1-1a), to specifically and quantitatively detect the concentration of target antigens. For instance, the antigen could be a critical protein for diagnosing human disease. In a typical “sandwich” ELISA process, a known quantity of capture antibodies are bound to a polystyrene microplate surface. Then antigen-containing sample (e.g. serum) is added to the plate. The target antigens in the sample will bind specifically to the capture antibodies and be immobilized whereas the unbound antigens (non-targets) will be washed away. Enzyme-linked detection antibodies are then applied which also bind specifically to the target antigens. After the unbound enzyme-linked antibodies are washed away, a chemical is applied which is converted by the enzyme into a color or fluorescent signal. The quantity of the target antigens can be determined by measuring the absorbency or fluorescence of the sample.

Optical detection is generally regarded as the gold standard in laboratory settings. However, conventional optical detection systems are very difficult to integrate into POC applications [2]. Recently magnetic immunoassays (MIA) emerged as an alternative solution [3-5]. The steps of MIA are illustrated in Figure 1-1b. The first two steps resemble those in ELISA. In the third step, magnetic beads conjugated with detection antibodies are introduced and bind specifically to the target antigens. After the unbound beads are washed, the magnetic field from the remaining beads is detected by embedded magnetic sensors as an indication of the concentration of target antigens.

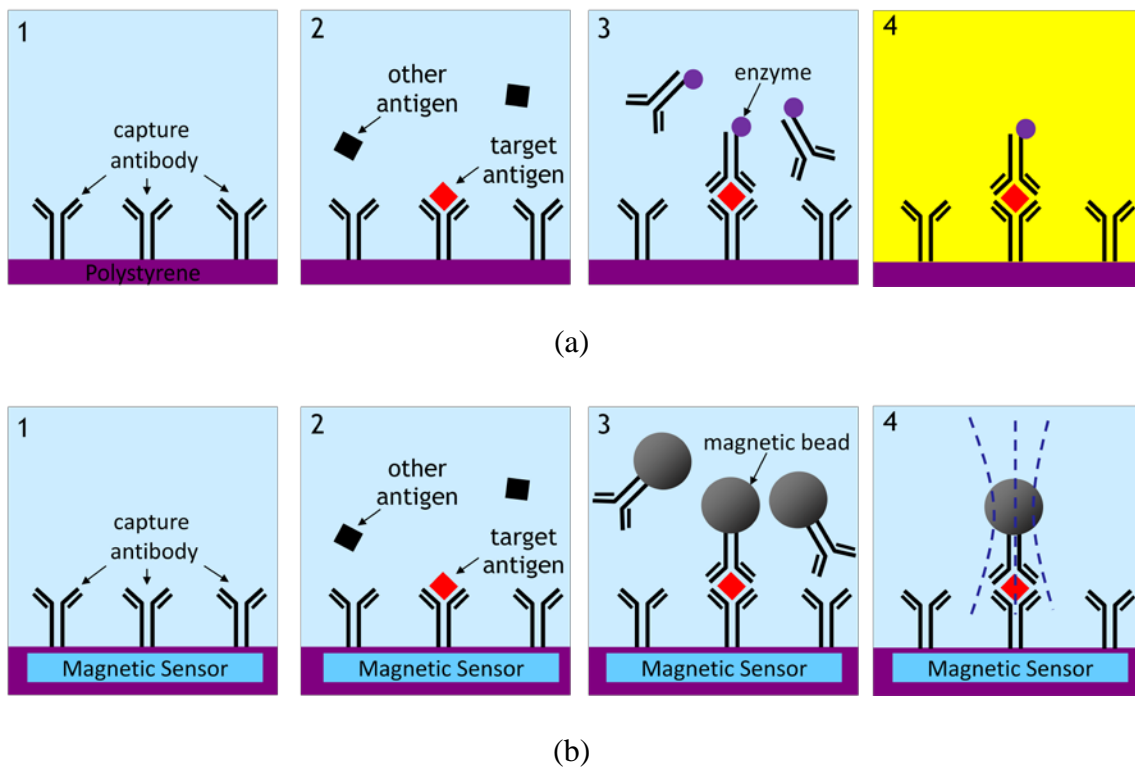


Figure 1-1: Comparison of conventional (optical) and emerging (magnetic) assays. (a) "Sandwich" enzyme-linked immunosorbent assays (ELISA) and (b) magnetic immunoassays (MIA)

It is important to note that the major differences between ELISA and MIA are the labeling and detection steps. In MIA, the target antigens are labeled by magnetic particles and the signal to be detected is the magnetic field of the labels, whereas in ELISA, the targets are chemically labeled and the signal is the absorbency or fluorescence of the sample. Magnetic labels have the advantages of remote manipulation [6] and being more chemically stable than their enzymatic counterparts. Moreover, low magnetic background in biological samples makes it possible to detect target analytes with high sensitivity. Most importantly, the magnetic detection eliminates the requirement for complex and bulky optical instrumentation and therefore is suitable for POC applications.

This dissertation focuses on the engineering aspects for a magnetic diagnostic tool and describes how a compact and robust magnetic label detector is built. It starts with the properties of magnetic labels and then proposes a novel label detector. Next the

challenges to build this detector are analyzed. Finally system solutions and circuit implementation are provided and discussed.

The dissertation is organized as follows. In Chapter 2, magnetic properties of microbead labels are analyzed. Prior works on magnetic label detection are reviewed followed by a comparison of two label detection methods. In Chapter 4, design challenges of a CMOS magnetic microbead relaxation detector, as well as corresponding solutions are discussed. System architecture and detailed circuits of the CMOS bead detector are described in Chapter 5. Measurement results of bead relaxation are shown in Chapter 6. Conclusions and future research directions are discussed in Chapter 7.

The CMOS chip described in this dissertation is the first magnetic label detector reported in the literature that does not require any external magnet, reference cell or field calibration. It detects and distinguishes magnetic labels based on their relaxation characteristics with a resolution more than 1000x better than that achieved by state-of-the-art sensors. Its compactness, scalability and robustness make the CMOS magnetic bead relaxation detector very competitive for point-of-care biomedical applications.

## Chapter 2

# Magnetic Label Detection

Requirements of diagnostic test for resource-limited settings can be abbreviated with the acronym ASSURED [1]: Affordable, Sensitive, Specific, User-friendly, Rapid, Equipment-free<sup>a</sup> and Deliverable. Therefore an ideal magnetic label detector should be an inexpensive and portable system that performs rapid, sensitive and robust detection unaffected by environment variation. In this chapter, we will briefly discuss the properties of the magnetic labels and then review the technologies and methods for magnetic label detection published in the past decade.

## 2.1 Magnetic Labels

Magnetic microbeads and nanoparticles have been widely used in biomedical applications [7], such as cell separation and medical imaging. In emerging magnetic bioassays, magnetic particles are used to label target analytes. Compared to magnetic nanoparticles (MNPs), microbeads (1 - 4.5  $\mu\text{m}$ ) have the advantages of being readily manufactured with uniform diameter and spherical shape, well controlled in magnetic properties, and easily observed with optical microscopy techniques. In the experiments described in this dissertation, commercially available Dynabeads® (Invitrogen Inc, Oslo, Norway) are used to demonstrate single label detection for applications in high-sensitivity bioassays.

Dynabeads consist of iron oxide ( $\text{Fe}_2\text{O}_3$ ) MNPs dispersed in a polymer matrix (Figure 2-1) [8]. The MNPs are superparamagnetic, meaning that they only show magnetic properties in the presence of an external magnetizing field (Figure 2-2). Unlike

---

<sup>a</sup> i.e. no large electricity-dependent instrument

ferri-magnetic or ferro-magnetic particles, there is no remnant field when the external field is removed and therefore the beads do not attract each other or agglomerate.

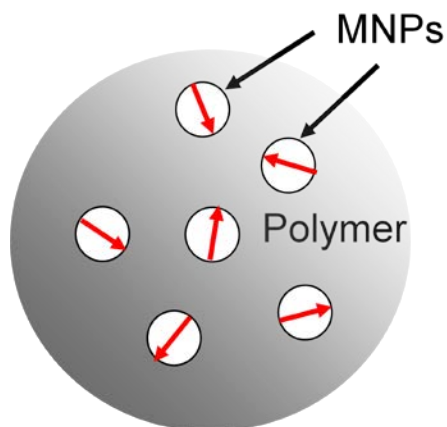


Figure 2-1: Composition of a Dynabead. Each bead consists of magnetic nanoparticles (MNPs) dispersed in a polymer matrix.

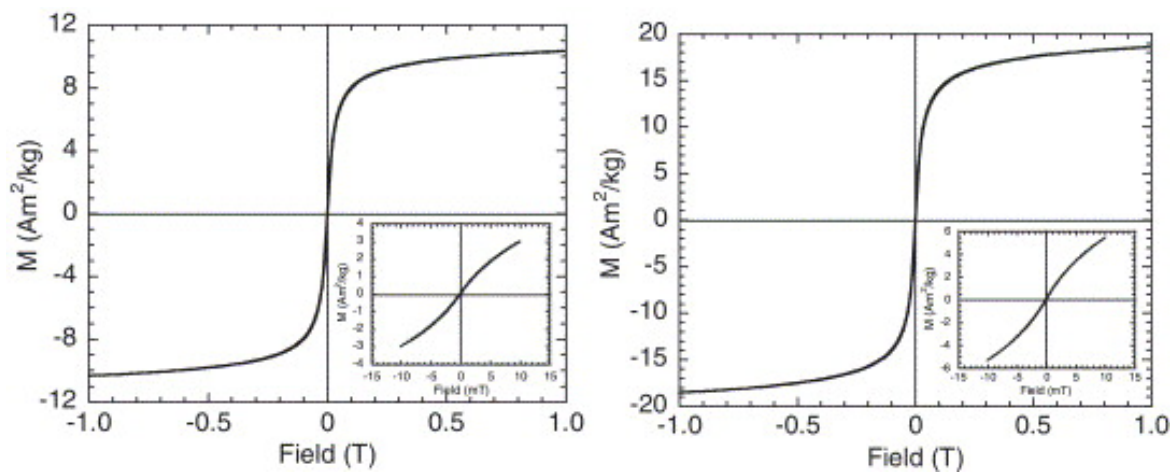


Figure 2-2: Magnetization versus magnetic field at room temperature for M-280 (left) and M-450 (right) in the field range of ( $\pm 1$  T) [7]. Inset figures show the magnetization curves at low-field ( $\pm 10$  mT).

Table 2-1: Characterization Results of Dynabeads<sup>b</sup> [8].

<i>Bead</i>	$D_b$ ( $\mu\text{m}$ )	<i>CV</i> (%)	$\rho$ ( $\text{g}/\text{cm}^3$ )	$P_{Fe/b}$ ( $\text{mg}/\text{g}$ )	$\chi_m$ ( $10^{-5}\text{m}^3/\text{kg}$ )	$M_0$ ( $\text{Am}^2/\text{kg}$ )	$M_s$ ( $\text{kA}/\text{m}$ )	$D_M$ ( $\text{nm}$ )
M-280	2.83	1.4	1.4	118	54	10.8	336	7.8
M-450	4.40	1.2	1.6	202	102	19.6	353	7.5
MyOne	1.05	1.9	1.7	255	81	23.5	336	7.4

Table 2-1 shows the bead parameters provided by the manufacturer [8]. The volume susceptibility  $\chi_0$  of a bead can be calculated from

$$\chi_0 = \frac{M}{H} = \frac{\rho m_b}{H \rho V_b} = \rho \chi_m \quad (2.1)$$

where  $V_b$  is the volume of the bead and  $m_b$  is bead magnetic moment which is equal to  $MV_b$  with  $M$  being bead magnetization. From Table 2-1, it can be derived that the susceptibilities of M-280, M-450 and MyOne beads are about 0.76, 1.63 and 1.38 respectively. It is important to note that the bead magnetization  $M$  is non-linear with the magnetizing field  $H$ , so bead susceptibility is actually dependent on magnetizing field. This can be verified from the beads' magnetization curves shown in Figure 2-2. At 5-mT magnetizing field, the magnetic moment density ( $m_b/\rho V_b$ ) is about 2  $\text{Am}^2/\text{kg}$  for M-280 beads and 3.5  $\text{Am}^2/\text{kg}$  for M-450, whereas at 10-mT magnetizing field, the magnetic moment density is 3  $\text{Am}^2/\text{kg}$  (M-280) and 5.5  $\text{Am}^2/\text{kg}$  (M-450).  $\chi_0$  is therefore about 0.7 (M-280) and 1.4 (M-450) when magnetizing field is 5 mT, which is close to the value calculated from Table 2-1, but drops to 0.52 (M-280) and 1.1 (M-450) when the magnetizing field increases to 10 mT. In point-of-care applications, low-field operation is usually required in order to meet power consumption specifications. For the experiments in this dissertation, the magnetizing field is around 3 mT, so the susceptibilities calculated from Table 2-1 will be used.

---

<sup>b</sup> *CV* is the standard deviation of the bead diameter  $D_b$ , given as percentage of the mean bead diameter;  $\rho$  is the bead density;  $P_{Fe/b}$  is the iron content in bead in mass percentage;  $\chi_m$  is the initial mass magnetic susceptibility determined from the magnetic analysis;  $M_0$  is the mass saturation magnetization of the beads;  $M_s$  is the intrinsic spontaneous magnetization of the MNPs in the beads and  $D_M$  is the MNP diameter determined by high-field magnetic analysis.

The MNP diameter is an important parameter to estimate the superparamagnetic properties of the beads.  $D_M$  in Table 2-1 was calculated by fitting a bead's magnetization curve in high magnetizing field [8]; however, it does not fully reflect the bead's properties in low field. An estimate of the MNP size can be performed with the following weak-field analysis.

Assuming the MNPs in a bead are monodisperse and there is no interaction between the MNPs, then the magnetic moment  $m_b$  of the bead is given by

$$m_b(H) = Nm_0L\left(\frac{\mu_0m_0H}{k_B T}\right) \quad (2.2)$$

where  $N$  is the total number of MNPs in a bead;  $m_0$  is the magnetic moment of each MNP given by

$$m_0 = M_s V_{MNP} \quad (2.3)$$

where  $M_s$  is the MNP saturation magnetization and  $V_{MNP}$  is the volume of MNP core;  $\mu_0$  is the vacuum permeability;  $H$  is the magnetizing field;  $k_B$  is the Boltzmann constant;  $T$  is the temperature in Kelvin and  $L$  is the Langevin function

$$L(x) = \coth(x) - \frac{1}{x} \quad (2.4)$$

In low magnetic field when

$$\mu_0m_0H \ll k_B T \quad (2.5)$$

Eq. (2.4) becomes

$$L(x) \approx \frac{x}{3} \quad (2.6)$$

So Eq. (2.2) can be rewritten as

$$m_b = \frac{\mu_0 N m_0^2 H}{3k_B T} \quad (2.7)$$

Eq. (2.7) shows that in weak field, the bead's magnetic moment is linear with magnetizing field  $H$  and inversely proportional to temperature, which is similar to the paramagnetism given by Curie's law.

From Eq. (2.1) and Eq. (2.7), DC susceptibility  $\chi_0$  can be rewritten as

$$\chi_0 = \frac{m_b}{V_b H} = \frac{\mu_0 M_S^2 N V_{MNP}^2}{3 k_B T V_b} \quad (2.8)$$

Eq. (2.8) shows that in weak field, the bead susceptibility is independent of magnetizing field.

The iron content in a bead can be expressed as

$$P_{Fe/b} = \frac{N \rho_{MNP} V_{MNP}}{\rho_b V_b} P_{Fe/Fe_2O_3} \quad (2.9)$$

where  $\rho_{MNP}$  is the MNP density, which is approximated by  $Fe_2O_3$  density ( $5.2 \times 10^3 \text{ kg/m}^3$ ).  $P_{Fe/Fe_2O_3}$  is the iron content in  $Fe_2O_3$ , which is 70%.

With Eq. (2.8), (2.9) and the measured parameters given in Table 2-1, the MNP size is estimated to be 12.5 nm (MyOne) and 14nm (M450 and M280). These values are larger than  $D_M$  listed in Table 2-1, where bead diameter is extracted by curve fitting bead magnetization in strong field [8]. The method used in [8] is an estimate of the average size of MNPs in a bead; however, it does not reflect MNP size distribution.

To show the difference between the two estimation methods, a simulation is run on four beads with same saturation magnetic moment but different MNP composition. Bead 1 has two 12-nm MNPs inside and Bead 2 consists of sixteen 6-nm MNPs. Bead 3 has one 12-nm MNP and eight 6-nm MNPs whereas Bead 4 contains nine MNPs all of which are 7.3 nm.

The simulation results are plotted in Figure 2-3. Bead 1 and Bead 2 can be clearly distinguished from each other based on their high-field magnetization since the average MNP size in the two beads is different. For Bead 3 and Bead 4, since they have the same average MNP size, it is difficult to distinguish them with the strong-field analysis; however, their low-field response is quite different and can be used to analyze MNP composition. The low-field analysis is based on susceptibility fitting. As shown in Eq. (2.8), the susceptibility of a bead is proportional to  $N V_{MNP}^2$  for monodisperse MNPs and is more sensitive to large MNPs if a bead contains MNPs that have different sizes. As reported in [8], some of the MNPs in the Dynabeads form clusters in the 20nm range and individual MNPs are estimated to have size distribution from 6-12 nm. So the susceptibility analysis above is actually a good estimate of the upper bound of MNP size distribution in Dynabeads.

Eq. (2.5) shows that the magnetizing B-field should be much less than 13 mT for 12-nm MNPs in the Dynabeads. To meet this low-field requirement, the magnetizing field used in the experiments in this dissertation is chosen to be around 3 mT.

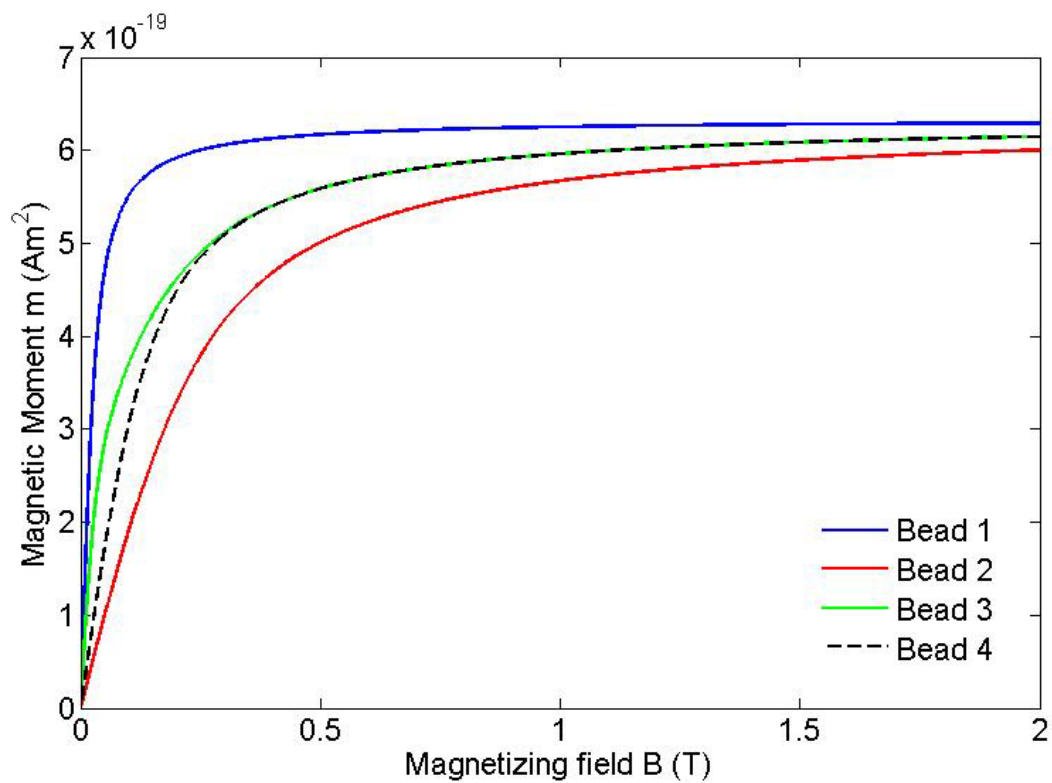


Figure 2-3: Simulated bead magnetization dependence on MNP size distribution. Four beads with the same saturation magnetic moment are simulated. Bead 1 contains two 12-nm MNPs; Bead 2 consists of sixteen 6-nm MNPs; Bead 3 consists of half of Bead 1 and Bead 2 (one 12-nm MNP and eight 6-nm MNPs) whereas Bead 4 has the same number of MNPs as Bead 3, but all MNPs are identical (7.3 nm). The magnetization curves are plotted based on Eq. (2.2) and Eq. (2.3) with  $M_s = 350$  kA/m and  $T = 300$  K.

## 2.2 Detectors

Figure 2-4 shows a cross section of a typical magnetic label detection platform. The bead is magnetized by a magnetizing B-field  $B_{mag}$ . The induced magnetic field from the bead  $B_{bead}$ , is detected by a magnetic sensor and converted to an electrical signal.

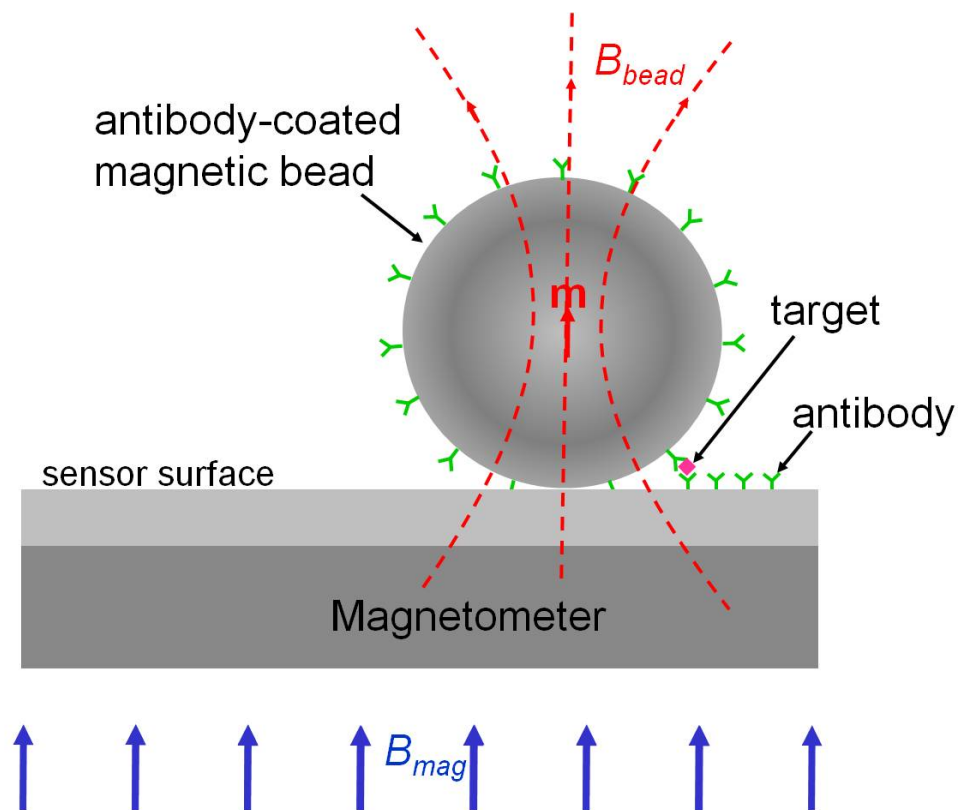
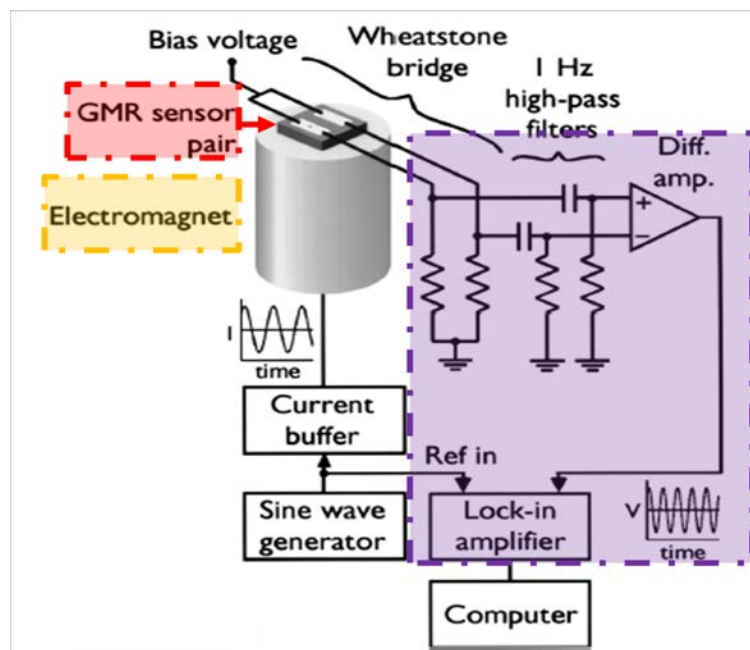


Figure 2-4: Cross section of a typical magnetic label detector.

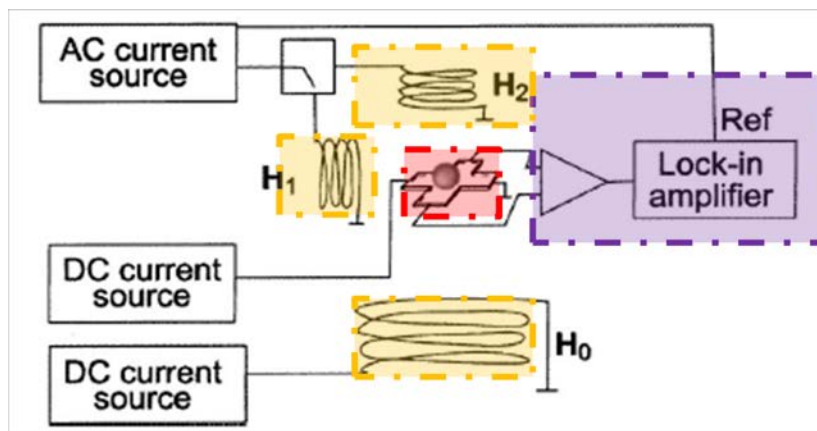
Various magnetic label detectors have been reported [5, 9-13] based on Superconducting Quantum Interference Devices (SQUID) [10], Hall-effect sensors [9, 13] or Giant Magnetoresistance (GMR) sensors [5, 11, 12]. Figure 2-5 shows two examples of the magnetic bead detectors implemented with miniaturized magnetic sensors that achieve single bead detection resolution, which is essential for high-sensitivity bioassays. The first one is Bead Array Counter (BARC) developed by the Naval Research Lab [5]. It consists of multi-layer GMR sensors, an electromagnet controlled by a waveform generator and a readout channel formed by a filter network and lock-in amplifier. The second detector was developed by EPFL, which was implemented with a Hall-effect sensor, magnetizing coils and bench-top amplifiers [9]. Clearly in each of the two examples, there are three building blocks – magnetic sensors, magnetizing field generators and readout electronics. The building blocks in the label detectors developed by NRL and EPFL, however, are not suitable for point-of-care applications. Both detectors are implemented with bulky, power-hungry and expensive electromagnets and bench-top readout equipment. The cost of the BARC detector is also driven up by the complex and special sensor fabrication process.

Recently magnetic bead detectors integrated in standard CMOS technology have been reported [14, 15]. In both papers, microcoils are implemented on chip to generate the magnetizing field. In [14], Hall-effect sensors are embedded as magnetometers whereas in [15] on-chip LC resonant circuits consisting of the microcoils are used for bead detection. However, in both cases the area-efficiency and packing density is very low, partly due to the bead detection methods that will be discussed in the next section. In [15], the detection resolution may also be limited by spiral inductor size.

The detector implemented in this thesis is based on previous work from [14]. The entire magnetic label detector, including the electromagnets, the magnetometers and the readout electronics is integrated on a single 2.5 mm x 2.5 mm chip fabricated in a standard 0.18- $\mu\text{m}$  CMOS process, achieving a very high packing density and area efficiency.



(a)



(b)

Figure 2-5: Block diagrams of previous magnetic label detectors. (a) Bead Array Counter (BARC) by NRL [5] and (b) Hall-effect sensor by EPFL [9]. The three building blocks are highlighted (red: sensor; orange: magnetizing field generator; purple: readout electronics).

## 2.3 Detection Methods

Detecting the magnetic field from a bead in the presence of a much larger magnetizing field imposes stringent requirements on the detector's dynamic range, offset, linearity, and temperature stability. For example, a M-280 Dynabead in a 10-mT external field generates a field less than 20  $\mu\text{T}$  if measured 10- $\mu\text{m}$  away from the bead center. This induced magnetic field from the bead,  $B_{bead}$ , is more than 50 dB lower than the magnetizing field  $B_{mag}$  (the "baseline"). Previously published bead detection methods [14, 15] attempt to resolve a miniscule change from a bead superimposed on the much larger baseline (Figure 2-6). Since the baseline is sensitive to environmental variations, these solutions generally require reference sensors, baseline calibration and/or active temperature stabilization. These functional blocks, however, not only make the POC device less user-friendly, but also add significant penalty on chip area, power consumption and detection time.

One approach to overcome this problem is to apply the magnetizing field orthogonal to the sensitive axis of the sensor and detect the fraction of the bead response that is aligned with the sensitive axis [6-7]. Unfortunately, this solution suffers from several drawbacks. First, it requires precise alignment of the sensor to the magnetizing field. For example, a 60 dB rejection of the magnetizing field requires alignment accuracy better than 0.1 degrees. Moreover, the magnetizing field must be homogenous, thus requiring a significantly larger magnet and larger power dissipation than integrated solutions with on-chip magnetizing field generation.

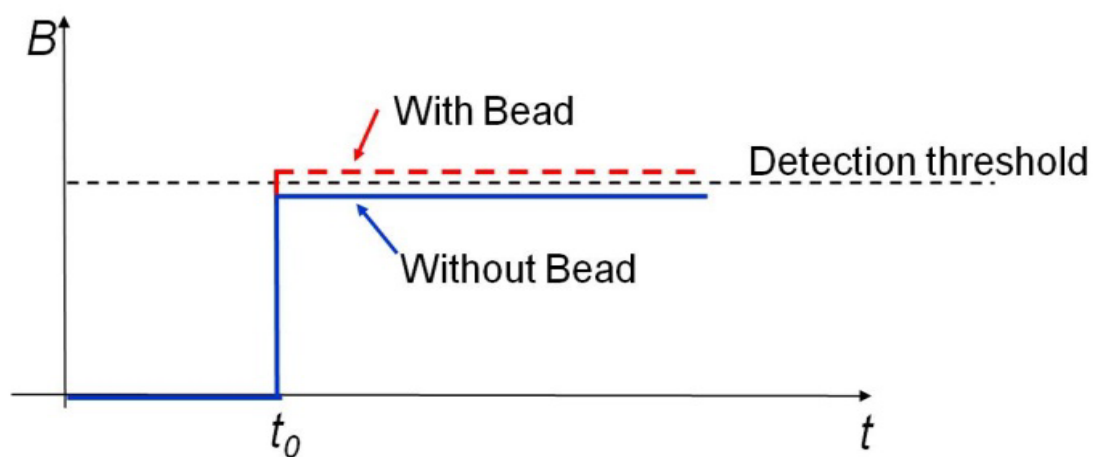


Figure 2-6: Conventional detection method based on bead magnetization

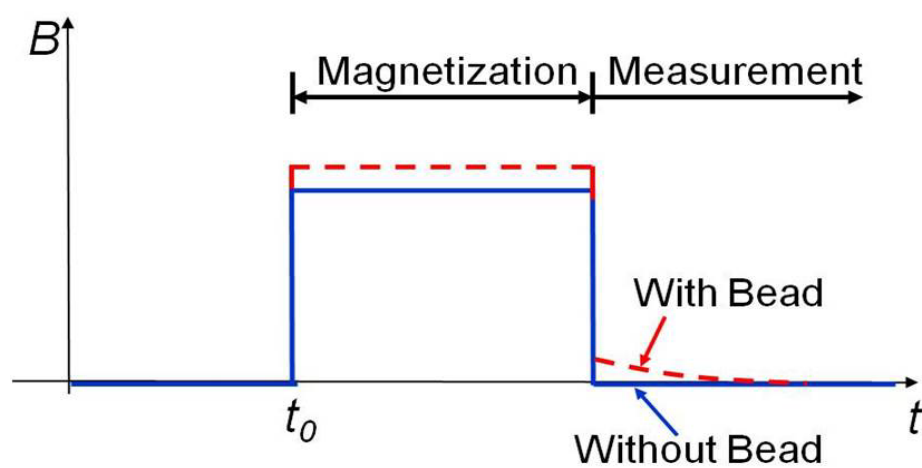


Figure 2-7: Detection method based on bead relaxation

The solution proposed in this dissertation avoids these drawbacks by detecting the magnetic relaxation signature from the label. As shown in Figure 2-7, the bead is first magnetized by a large field generated on-chip. The measurement starts after this magnetizing field is removed rapidly, thus eliminating the large baseline and detecting the decaying magnetic field from the bead. Prior demonstrations of relaxation field measurements relied on highly sensitive magnetometers such as SQUID and fluxgate sensors [4, 10] [16, 17]. Unfortunately these devices introduce a significant delay between the magnetization and measurement phases, resulting in reduced signal amplitude and increased measurement time. The solution described here leverages the short time constants and miniaturized components achievable in modern sub-micron CMOS technology. A fully integrated magnetic bead detector based on magnetic relaxation is demonstrated without requiring any external magnet, baseline calibration or reference sensor. The CMOS bead relaxation detector significantly reduces the power dissipation, detection time and system complexity while achieving high area-efficiency.

## 2.4 Summary

The magnetic property of a microbead is due to the magnetic nanoparticles (MNPs) in the bead. The size of MNPs can be estimated by susceptibility analysis. The bead susceptibility is independent with magnetizing field in low field and drops when magnetizing field increases. The low-field condition shown in Eq. (2.5) must be considered for bead detector design.

Three building blocks, including electromagnets, magnetic sensors and readout channels are required for a magnetic bead detector. Bead detectors with all building blocks implemented in CMOS process are compact, low-power and low cost and thus are promising for point-of-care applications.

A bead detection method based on the magnetic relaxation nature of MNPs is presented. Unlike conventional methods with beads detected during magnetization, it does not require large reference sensors, complex baseline calibration or active environment control. Therefore a CMOS bead detector based on magnetic relaxation is more area-efficient and robust in point-of-care settings.

## Chapter 3

# Magnetic Relaxation

The magnetic relaxation detection method gets rid of the baseline and therefore is more robust in point-of-care settings. It also relaxes dynamic range requirements on the system level and eliminates the needs for baseline calibration and reference sensors. So a detector based on magnetic relaxation is easier to operate and more area-efficient.

In this Chapter, we will first explore the origin of bead relaxation, followed by a discussion of how the bead relaxation is determined by its intrinsic properties. Finally a methodology of using frequency-domain relaxation measurement to optimize the bead detector design is presented.

### 3.1 Origin

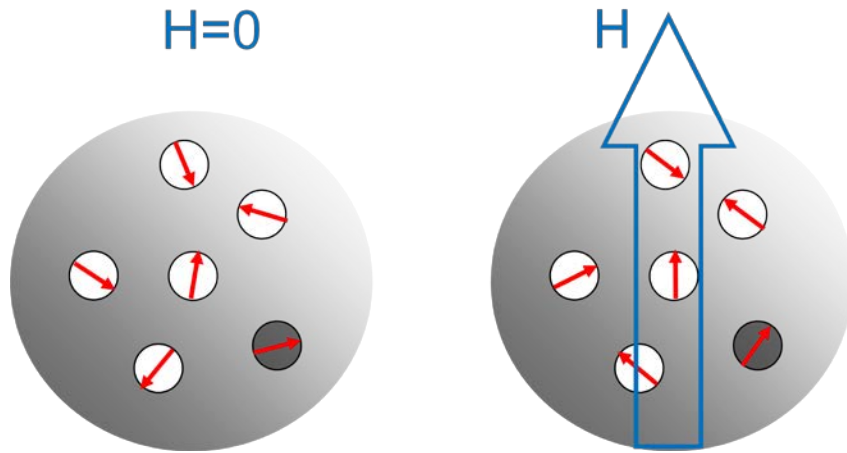
The magnetic relaxation of microbeads discussed in the previous chapter comes from the Néel relaxation of iron oxide MNPs in the microbead. Each MNP is modeled as a magnetic dipole. When no external field is applied, the dipoles are oriented along their easy axes where total magnetic energy is minimal. Since the easy axes of the MNPs are randomly distributed, the total magnetic moment of the bead is zero (Figure 3-1a). When a magnetizing field is applied, the dipoles align and the bead shows a net magnetic moment.

Now consider the case for a single MNP with a simple uniaxial easy axis (Figure 3-1b). Its magnetic energy in a magnetizing field is given by

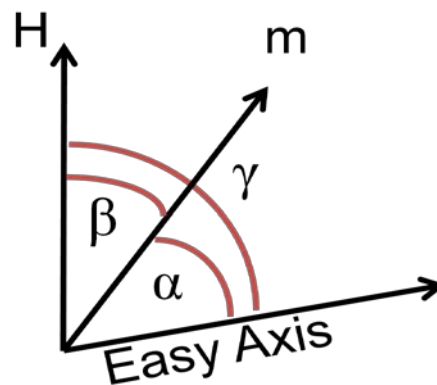
$$E = KV \sin^2 \alpha - \mu_0 m H \cos \beta \quad (3.1)$$

where  $K$  is the anisotropy constant which heavily depends on a MNP's magneto-crystalline structure and is also affected by shape and surface properties of the MNP;  $V$  is

the volume of the MNP;  $\alpha$  is the angle between the MNP's easy axis and its magnetic moment  $\mathbf{m}$  and  $\beta$  is the angle between  $\mathbf{m}$  and applied field  $\mathbf{H}$ .



(a)



(b)

Figure 3-1: Effect of the magnetizing field on MNPs. (a) Each MNP is considered a tiny magnet. When no external field is applied, the MNPs are randomly oriented. When an external field  $\mathbf{H}$  is on, the magnets tend to align with  $\mathbf{H}$ . (b) Magnetic moment  $\mathbf{m}$  of the MNP highlighted in (a), when  $\mathbf{H}$  is applied.  $\gamma$  is the angle between its easy axis and  $\mathbf{H}$  with a range of  $[0, \pi/2]$ .

The maxima and minima of the MNP's energy can be calculated from Eq. (3.1). Therefore an energy barrier exists when a MNP rotates its orientation. If the angle between the MNP easy axis and  $\mathbf{H}$  is defined as  $\gamma$  which has a range from 0 to  $\pi/2$ , then the height of the energy barrier is given by [18]

$$\Delta E = KV(1 - 2h(\sin \gamma + \cos \gamma)) \quad (3.2)$$

in a weak field where

$$h = \frac{H}{H_K} \ll 1 \quad (3.3)$$

with

$$H_K = \frac{2K}{\mu_0 M_s} \quad (3.4)$$

Figure 3-2 shows a simulation of the MNP magnetic energy as a function of  $\alpha$  and  $\gamma$  in the case of  $h = 0.1$ . Its minima occur approximately at  $\alpha = 0$  and  $\alpha = \pi$ , or along its easy axis and maxima around  $\alpha = \pm \pi/2$ . Therefore there are two energy barriers when the magnetic dipole rotates from 0 to  $2\pi$ . The total energy barrier is determined by the lower barrier which is given by Eq.(3.2). Assuming  $K$  is between  $2\sim 5 \times 10^4$  J/m<sup>3</sup> [19] and  $M_s$  is about 350 kA/m for Dynabeads, then the magnetizing B-field should be much less than 110 mT to meet the relaxation low-field requirement given by Eq. (3.3) and Eq. (3.4).

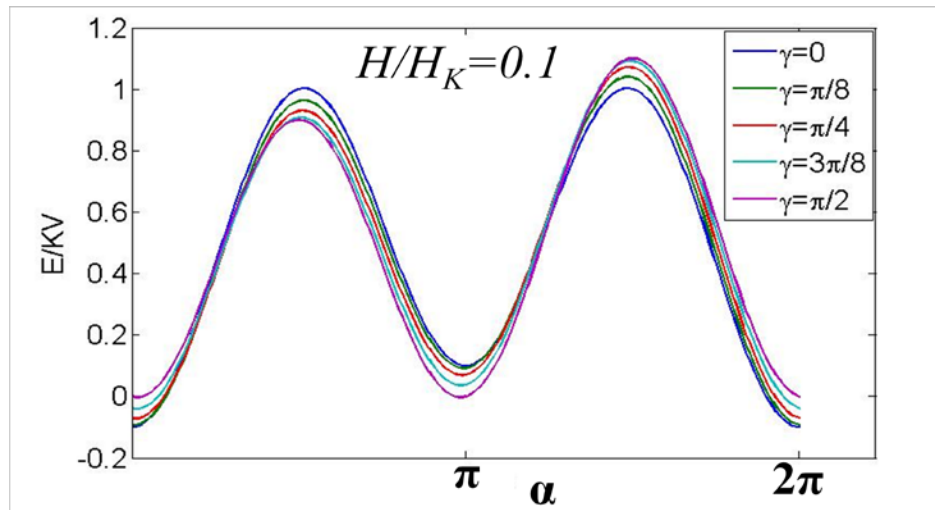


Figure 3-2: Simulated magnetic energy of a MNP with uniaxial easy axis in low magnetizing field.

So far we have ignored the thermal energy of the MNP. Thermal fluctuation may flip the dipole moment to cross the energy barrier with a time constant given by

$$\tau_{NH} = \tau_0 e^{\frac{[1-2h(\sin\gamma + \cos\gamma)]KV}{k_B T}} \quad (3.5)$$

Since the function  $f(\gamma) = \sin\gamma + \cos\gamma$  has a small variation (1 to 1.414) for  $\gamma$  in the range of  $[0, \pi/2]$ , the distribution of  $\tau_{NH}$  is narrow for random orientations of easy axes in small magnetizing field. Y using approximation  $f(\gamma) = 1$ , the Néel relaxation time constant in a magnetizing field given by Eq. (3.5) become independent of easy axis orientation and can be simplified into

$$\tau_{NH} = \tau_0 e^{\frac{(1-2h)KV}{k_B T}} \quad (3.6)$$

When the external field is removed ( $H = 0$ ), Eq. (3.6) turns into the well-known Néel relaxation expression

$$\tau_N = \tau_0 e^{\frac{KV}{k_B T}} \quad (3.7)$$

Eq. (3.7) shows that for a single MNP, there is no remnant field when no magnetizing field is applied, if the relaxation time constant is much shorter than the measurement time. Eq. (3.6) and Eq. (3.7) will be used throughout this dissertation for Néel relaxation, even though it is oversimplified by assuming an abrupt energy barrier. Further refined models for MNPs with uniaxial symmetry can be found in [20-22].

## 3.2 Magnetorelaxometry

It has been shown in Figure 2-7 that a bead can be detected based on its relaxation when the magnetizing field is removed abruptly. By including the relaxation dynamics given by Eq. (3.6) and Eq. (3.7), the bead's magnetic moment can be modified from Eq. (2.2) and it follows

$$m_b(H, t) = Nm_0 L\left(\frac{\mu_0 m_0 H}{k_B T}\right) \left(1 - e^{-\frac{t_m}{\tau_{NH}}}\right) e^{-\frac{t-t_m}{\tau_N}} \quad (3.8)$$

where  $t_m$  denotes magnetization time. The magnetic moment of a bead during magnetization and relaxation is shown in Figure 3-3.

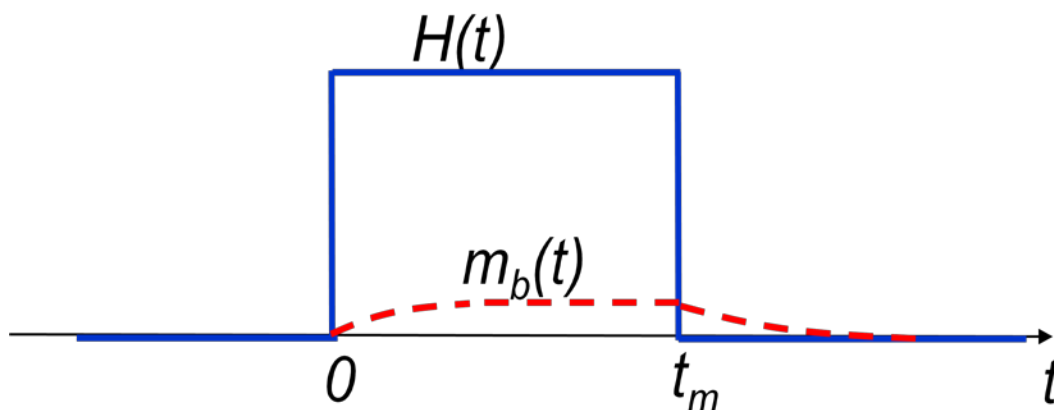


Figure 3-3: Bead magnetic moment in magnetization and relaxation

Eq. (3.8) shows that MNPs could be distinguished by their magnetic relaxation characteristics or magnetorelaxometry (MRX). Based on Eq. (3.6) and Eq. (3.7), MNPs of different sizes have different relaxation time constants. Consider a microbead consisting of only 10-nm and 8-nm MNPs. Assume  $h = 0.01$ ,  $K = 50 \text{ KJ/m}^3$ , and the 10-nm MNPs contributing to  $2/3$  of the bead's magnetic moment. From Eq. (3.7) the relaxation time constant of 10-nm and 8-nm MNPs are  $0.56 \mu\text{s}$  and  $0.025 \mu\text{s}$  respectively. If the magnetization time  $t_m = 5 \mu\text{s}$ , the MNPs are fully magnetized and the relaxation curve is first dominated by fast decaying of 8-nm MNPs then followed with the slower relaxation of 10-nm MNPs (Figure 3-4). By controlling the magnetization time, the relaxation dynamics is a reflection of MNPs enclosed in a microbead. When  $t_m = 0.05 \mu\text{s}$ , the magnetization time is too short for the 10-nm MNPs to be fully magnetized while enough for the 8-nm MNPs. The resulting relaxation is therefore dominated by the 8-nm MNPs.

Microbeads with different MNP compositions (size, material, etc) could also be distinguished by MRX techniques. This can be intuitively understood as if the bead discussed earlier splits into two beads, bead A and bead B, where bead A consists of all the 8-nm MNPs and bead B consists of all the 10-nm MNPs. Then the MRX techniques could be used to differentiate bead A and B. This could potentially lead to interesting applications such as multi-target magnetic assays.

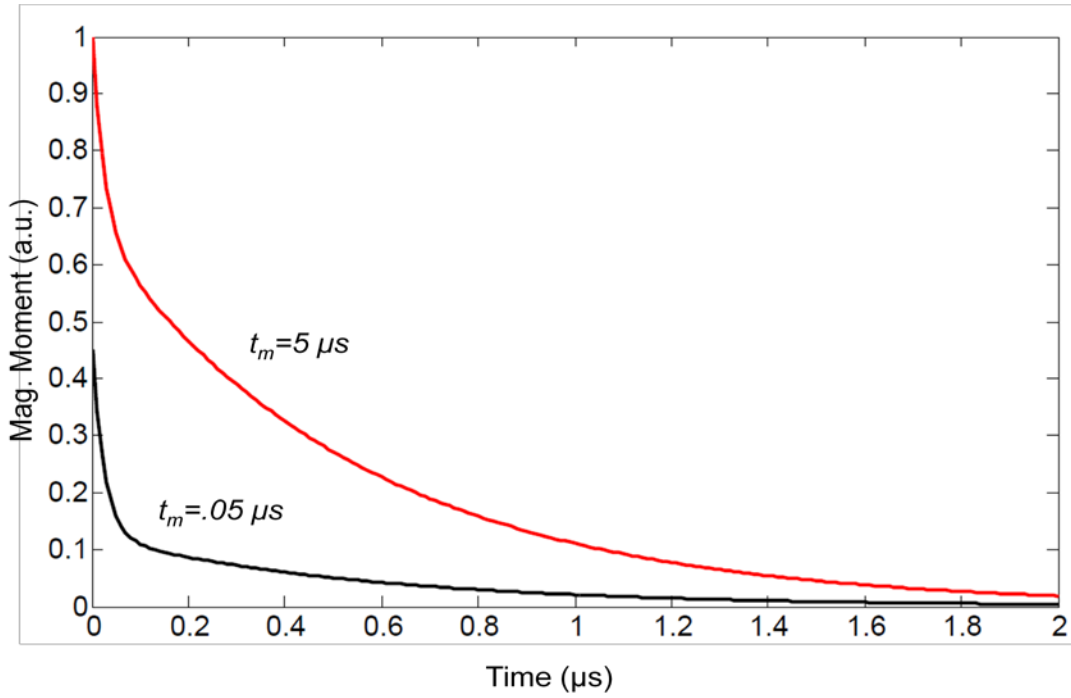


Figure 3-4: Simulated magnetic relaxation of a bead model with different magnetization time. The bead contains only 8-nm and 10-nm MNPs.

In real beads, the size distribution of the MNPs must be considered. Assuming all MNPs have the same saturation magnetization, the net relaxation signal is given by the moment superposition model [18]

$$m_b(H, t) = M_s \int_0^\infty V f(V) L(H, V) \left( 1 - e^{-\frac{t_m}{\tau_N(V)}} \right) e^{-\frac{t-t_m}{\tau_N(V)}} dV \quad (3.1)$$

where  $f(V)$  is the MNP volume distribution function.

To apply MRX technique on a bead with MNP size distribution, the magnetization time  $t_m$  can be precisely controlled and changed. When  $t_m$  is small, only the small MNPs with short  $\tau_N$  get magnetized and show relaxation; as  $t_m$  increases, the larger MNPs with longer  $\tau_N$  starts to contribute to the total relaxation. All the MNPs enclosed in a microbead could be detected and analyzed with this “scan” technique[23].

As we can see from Figure 3-4, it is important to start a MRX measurement as soon as the magnetizing field is removed, especially for small MNPs which have short relaxation time constant. Previous MRX measurements using Superconducting Quantum

Interference Devices (SQUID) [24] and fluxgate sensors [17, 25] suffer from a long delay (“dead zone”) of several hundred microseconds between switching off the magnetizing field and detecting the MNP field. This delay is set by the magnets and readout electronics and limits those instruments to the characterization of only MNPs with long relaxation time. With rapid switching and signal readout in integrated circuits, the CMOS magnetic relaxation detector designed for the experiments in this dissertation has a dead zone of less than 100 ns, which is more than three orders of magnitude improvement over that achieved on SQUID and flux-gate sensors. With significant improvement on detection resolution, CMOS MRX sensors enable a wide selection of MNPs and beads to be used as magnetic labels.

### 3.3 Complex Susceptibility

Néel relaxation of a bead can also be studied in the frequency domain by measuring its complex susceptibility [26]. Note Eq. (2.8) is only valid when magnetization time and measurement time are much longer than the Néel relaxation time constant  $\tau_N$ , and thus is called DC susceptibility. When the magnetization time is short, the equation no longer holds because the MNPs will not be fully magnetized. Instead it becomes frequency-dependent and may be modeled as

$$\chi(\omega) = \frac{\chi_0}{1 + j\omega\tau_N} \quad (3.2)$$

where  $\chi_0$  is the DC susceptibility shown in Eq. (2.8).

Complex susceptibility can also be rewritten in terms of real and imaginary components

$$\chi(\omega) = \chi'(\omega) - j\chi''(\omega) \quad (3.3)$$

Compare Eq.(3.3) to (3.2), we get

$$\chi'(\omega) = \frac{\chi_0}{1 + \omega^2\tau_N^2} \quad (3.4)$$

and

$$\chi''(\omega) = \frac{\omega\tau_N\chi_0}{1 + \omega^2\tau_N^2} \quad (3.5)$$

Figure 3-5 shows the simulated complex susceptibility of the microbead discussed in the previous section. There are two peaks in the imaginary susceptibility that are caused by the relaxation of 10-nm and 8-nm MNPs respectively. It can be shown that  $\chi''(\omega)$  peaked at

$$f_{max1,2} = \frac{1}{2\pi\tau_{N1,2}} \quad (3.6)$$

where  $\tau_{N1}$  and  $\tau_{N2}$  are the relaxation time constant of 10-nm and 8-nm MNPs, respectively.

The frequency-domain complex susceptibility originates from the same intrinsic properties of MNPs as the time-domain relaxation, therefore a complex susceptibility measurement can be used to model bead relaxation. The following example shows how a complex susceptibility measurement is applied to optimize the design of the relaxation detector.

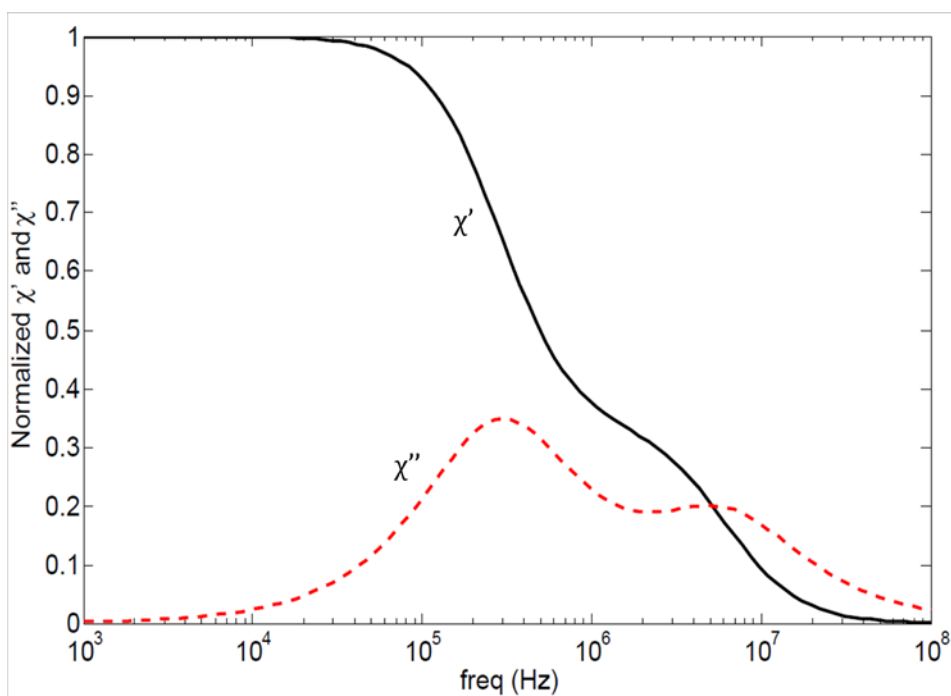


Figure 3-5: Simulated complex susceptibility for the bead model discussed in Section 3.2. The bead has only 8-nm and 10-nm MNPs.

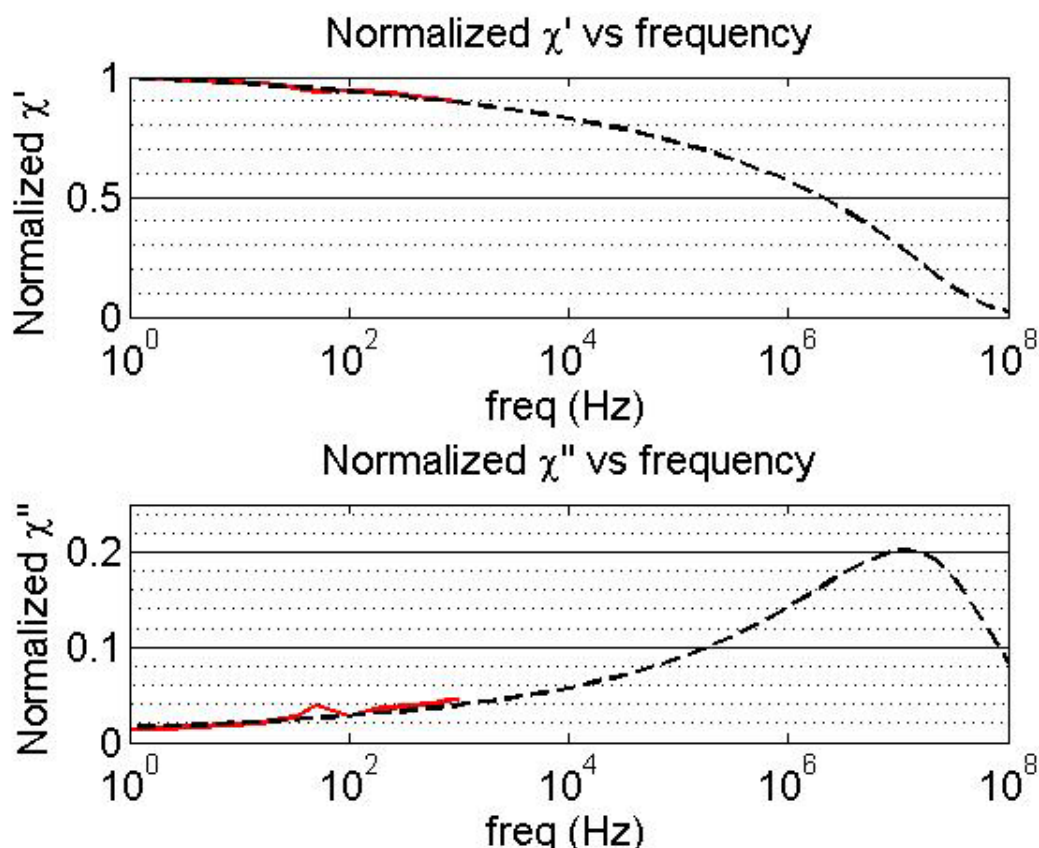


Figure 3-6: Real (top) and imaginary part (bottom) of the measured (red) and projected (black) complex susceptibility on Dynabeads M-450. The values are normalized to DC susceptibility.

The complex susceptibility of Dynabeads M-450 beads is measured with Quantum Design MPMS-XL SQUID magnetometer (San Diego, CA) and the results are shown in Figure 3-6. Due to equipment limit, the measurement frequency only goes up to 1 kHz. But the measurement still gives some hints about the intrinsic properties of the bead. The imaginary susceptibility has a peak around 50 Hz that is likely due to the clusters formed in the bead that are about 20-nm [8]; however, the imaginary susceptibility does not reach its maximum until around 1 kHz and still in an uptrend. To explore the bead relaxation at frequency higher than 1 KHz, the complex susceptibility measurement is curve fitted by a Dynabead model which assumes anisotropy constant  $K = 50 \text{ KJ/m}^3$  and the MNP volume  $V_{\text{MNP}}$  follows a log-normal distribution

$$f(V_{MNP}) = \frac{1}{\sqrt{2\pi}\sigma V_{MNP}} \exp\left\{-\frac{(\ln V_{MNP} - \ln u)^2}{2\sigma^2}\right\} \quad (3.7)$$

where  $u$  is the mean volume and  $\exp(\sigma)$  is the standard variation.  $u$  can be calculated as the mean MNP diameter of Dynabeads is measured to be about 8 nm [8] and  $\sigma$  is extracted to be 0.39 from the fitting. With the MNP size distribution, Eq. (2.8), Eq. (3.2) and the moment superposition model [18], the projected complex susceptibility of Dynabeads is plotted over a frequency range of 1 Hz to 100 MHz in Figure 3-6. The simulation shows the imaginary susceptibility peaks around 10 MHz, which corresponds to the relaxation time constant of 8-nm MNPs.

To detect a bead, we would like to minimize the probability of detection error or signal-to-noise ratio if the detection time is fixed. Therefore two key questions to answer are how to choose magnetization time  $t_m$  and when relaxation measurement should start. The related parameters are shown on a relaxation graph (Figure 3-7) where  $V_s$  denotes the bead signal measured at  $t_s$ . Shorter  $t_m$  will reduce total measurement time, but it also implies smaller bead signal since larger MNPs in the bead will not be magnetized as discussed in Section 3.2. For the relaxation signal that decays quickly, it is desired to measure it as soon as the magnetizing field is switched off; however smaller  $t_s$  requires larger bandwidth and thus more white noise will be added. So the optimized magnetization and sampling time are chosen to maximize the following figure of merit

$$FOM = \frac{SNR}{t_{measure}} \propto \frac{V_s^2 t_s}{t_m} \quad (3.8)$$

With the bead model, bead relaxation for different magnetization time  $t_m$  is simulated and a FOM contour is plotted with various  $t_m$  and  $t_s$  (Figure 3-8). The optimized FOM is achieved around  $t_m \sim 256$  ns and  $t_s \sim 32$  ns, even though the optimization is shallow. Therefore in this design, the minimum  $t_m$  is chosen as 256 ns and -3dB bandwidth is chosen as 16 ns. The maximum  $t_m$  is 256  $\mu$ s so the wide range of magnetization time will allow detecting relaxation of MNPs in various sizes.

For the complex susceptibility measurement, frequency higher than 1 kHz can't be measured by the SQUID magnetometer, which causes measurement frequency discrepancy between the complex susceptibility and relaxation and thus a bead model is required to fit the measurement. This issue, however, can be resolved by using on-chip inductors and network analyzer which will extend complex susceptibility measurement to a much wider frequency range so the bead relaxation can be projected by an inverse-Laplace transform directly.

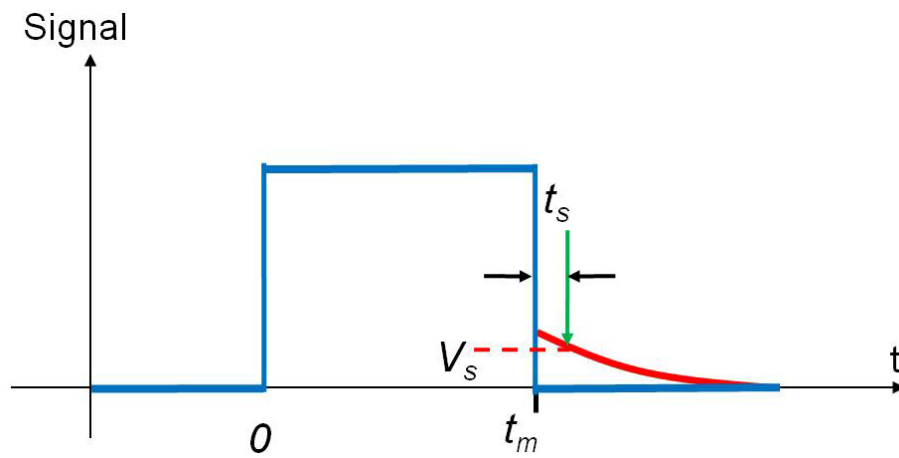


Figure 3-7: Parameters in bead relaxation that affect SNR and measurement time

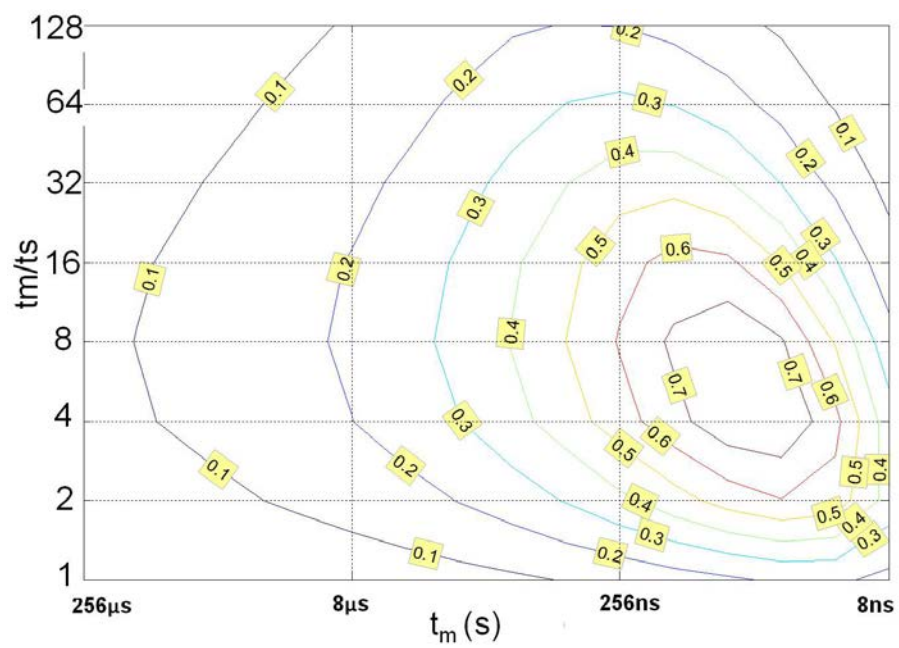


Figure 3-8: Contour plot of FOM vs. magnetization time and sampling time

## 3.4 Summary

Magnetic relaxation of a MNP originates from thermal fluctuations that flip the magnetic dipole moment to overcome an intrinsic energy barrier. The relaxation time constant strongly depends on the height of the energy barrier, which is proportional to MNP volume.

CMOS magnetorelaxometry (MRX) sensors have the advantage of high resolution and can detect relaxation of a wide range of MNPs in a bead, including small MNPs that have relaxation time constants of nanoseconds. By measuring a bead's relaxation with well controlled magnetization time, MNPs of different sizes in a bead are "scanned" and thus the composition of the bead can be analyzed. CMOS MRX sensor also enables differentiation of MNPs and beads based on their relaxation characteristics.

Complex susceptibility is the measurement of magnetic relaxation in frequency domain. It is a powerful tool to model a bead's time-domain relaxation through an inverse-Laplace transform. Complex susceptibility of Dynabead M-450 beads is measured and curve fitted. Magnetization time and readout channel bandwidth are chosen based on optimized signal-to-noise ratio and measurement time, as well as flexibility to detect relaxation of various MNPs.

## Chapter 4

# Design Challenges and Solutions

As we discussed earlier, Hall-effect sensors are amenable to integration and hence enable very compact and low cost systems. In this chapter, an introduction to CMOS Hall-effect sensors is presented first. Then the challenges by using these miniaturized sensors for bead relaxation measurement are discussed, followed by corresponding solutions.

### 4.1 Hall Effect

The basic physical principle underlying the Hall effect is the Lorentz force [27] as shown in Figure 4-1. For a thin and long conducting plate carrying current, when a magnetic field  $B$  that is perpendicular to the plate is applied, the Lorentz force will deviate carriers (electrons in this case) from their paths and a Hall voltage  $V_H$  appears between the point electrical contacts at its periphery described by

$$V_H = G_H \mu_H B V_{bias} \frac{W}{L} \quad (4.1)$$

where  $W$  and  $L$  are the width and length of the plate;  $\mu_H$  is the Hall mobility of the majority carriers and is approximated by carrier drift mobility  $\mu_n$  when in weak field ( $\mu_n B \ll 1$ );  $V_{bias}$  is the bias voltage applied to the plate;  $G_H$  is the geometrical correcting factor for finite-size Hall devices, which is close to 1 for very long Hall device, about 0 for very short Hall device and  $\sim 0.7$  for  $L \approx W$  [27].

As seen from Eq. (4.1), the Hall voltage is linear with applied magnetic field  $B$  and bias voltage  $V_{bias}$ , therefore the voltage-related sensitivity can be defined as

$$S_V = \left| \frac{V_H}{V_{bias} B} \right| = G_H \mu_H \frac{W}{L} \quad (4.2)$$

Voltage-related sensitivity is strongly dependent on carrier mobility. Typical values of  $S_V$  for semiconductor Hall devices vary from  $3 \text{ T}^{-1}$  for InSb to less than  $0.1 \text{ T}^{-1}$  in silicon [27]. In standard CMOS processes, Hall plates can be realized either with a diffusion layer (e.g. N-Well) or the channel region of a transistor. In this prototype, N-Well Hall-effect sensors are chosen due to their higher carrier mobility ( $\sim 670 \text{ cm}^2/\text{V/s}$ ).

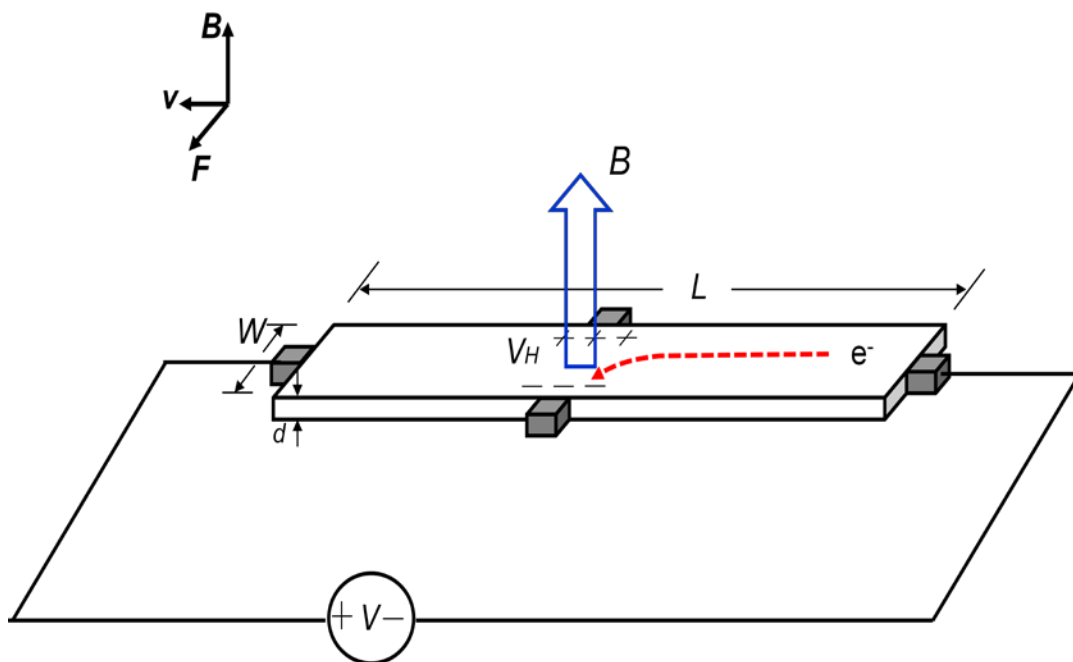


Figure 4-1: The working principle of a Hall plate. The basic physical principle underlying the Hall effect is the Lorentz force.

## 4.2 Post-processing

The technology used to fabricate the chip is a standard 0.18- $\mu\text{m}$  CMOS process. Since in typical multilayer metal processes, the chip surface is as much as 10  $\mu\text{m}$  above the active devices and the magnetic signal from the bead decreases with the third power of distance, a simple post-processing step is used to remove the second layer of metal and all the interlayer dielectric (ILD) material above it in the sensor area (Figure 4-2). The sensor area and CMOS IC area are protected with metal layers as a hard mask for RIE. The hard mask is then removed in a wet etching step. Photo resist is used to protect the pad area from etching. The post processing does not require extra masks and can be performed on the wafer level.

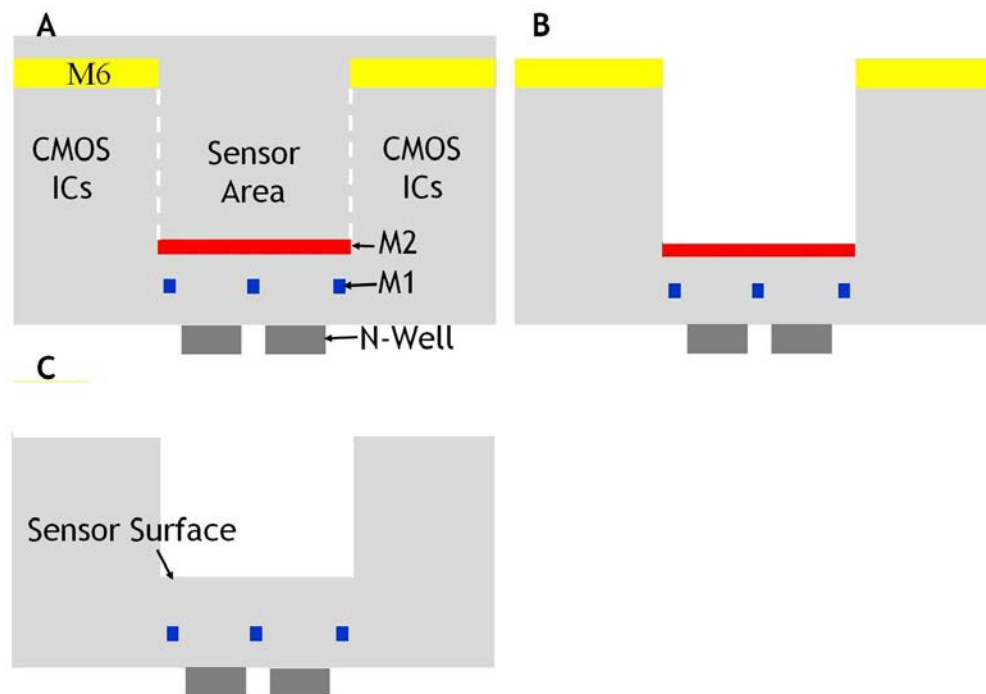


Figure 4-2: Post-processing steps. A) Original chip fabricated by CMOS foundry; B) ILDs removed by RIE with metal layers serving as masks; C) Metals layers removed by wet etching and sensor surface created.

After the post processing, there is only one layer of metal and polysilicon for interconnects in the sensor area, which imposes layout challenges. Figure 4-3 shows a cross section of the entire detection platform after post processing. A current  $I_{mag}$  passing through a pair of metal wires on both sides of the N-Well Hall-effect sensors generates the magnetizing field  $B_{mag}$ . The induced magnetic field from the bead,  $B_{bead}$ , is detected by the embedded Hall-effect sensor and converted to an electrical signal for processing. The sensor surface is  $3\text{-}\mu\text{m}$  from the embedded Hall-effect detectors and  $1.1\text{-}\mu\text{m}$  from the current-carrying wires.

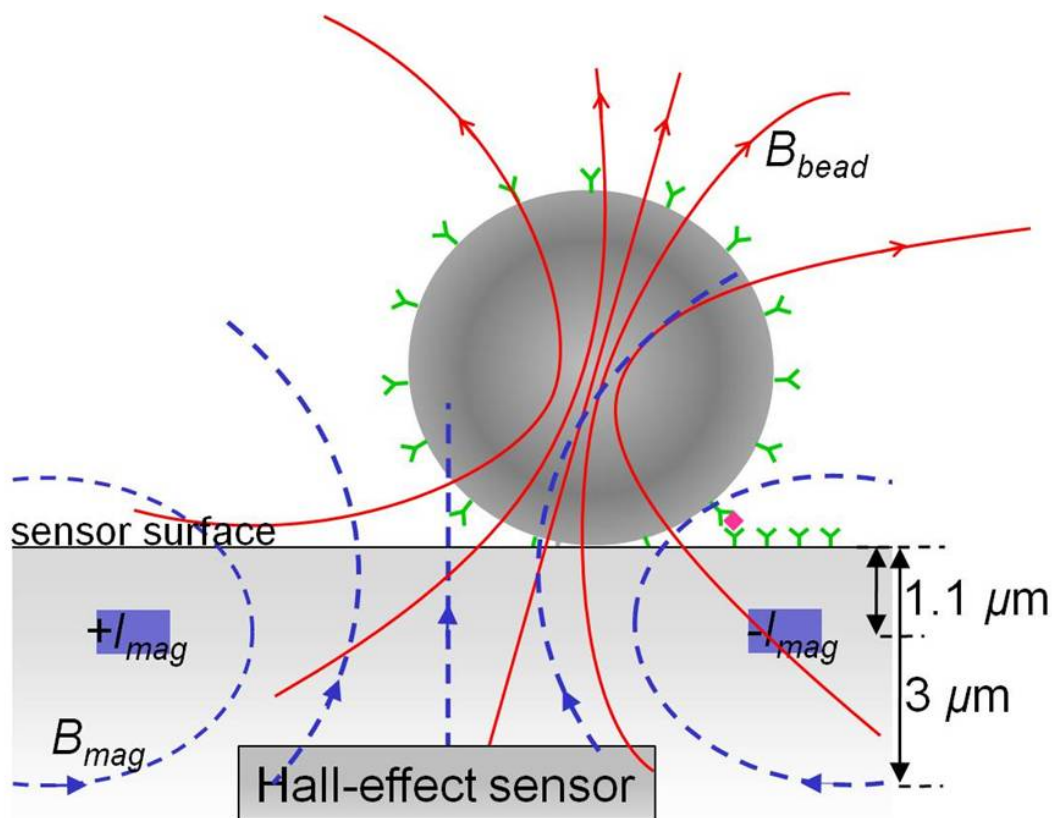


Figure 4-3: Cross section and working principle of a CMOS magnetic label detector

### 4.3 Design Challenges

The post processing brings bead closer to sensor and increases the signal. However, the resulting bead signal is still very small. In this chapter, we are going to analyze the bead signal and error sources.

To calculate the bead signal, each MNP in the bead needs to be considered as a dipole. Then the induced magnetic field from each MNP is calculated and summed at each point of the sensor. The moment superposition model is more accurate but not very efficient for calculation. Instead we use a simple model where the whole bead is considered as one dipole. This approach underestimates the microbead signal by less than 30% from the moment superposition model.

As shown in Figure 4-4, two long wires at  $x = X_W$  and  $-X_W$  carrying current  $I_{mag}$  in opposite direction. The bead center is located at  $(X_b, 0, Z_b)$ . The magnetizing field at the bead center is given by

$$\mathbf{H} = \frac{H_0}{(P^2 - 4\alpha^2)} [2\alpha\beta\hat{\mathbf{x}} + (1 - \alpha^2 + \beta^2)\hat{\mathbf{z}}] \quad (4.3)$$

where

$$\alpha = \frac{X_b}{X_W} \quad (4.4)$$

$$\beta = \frac{Z_b}{X_W} \quad (4.5)$$

$$H_0 = \frac{I_{mag}}{\pi X_W} \quad (4.6)$$

$$P = 1 + \alpha^2 + \beta^2 \quad (4.7)$$

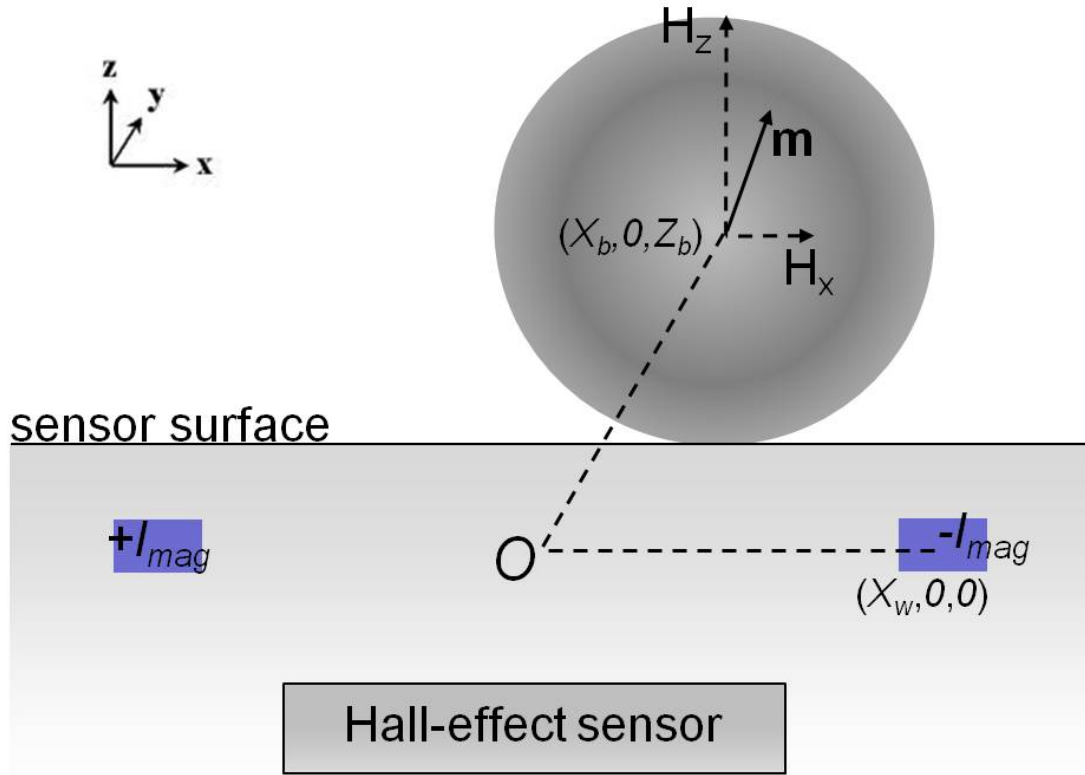


Figure 4-4: Bead detector model for an easy calculation of magnetizing field. The magnetizing field is generated by a pair of long wires carrying current  $I_{mag}$  in opposite directions.

When a bead is located between the two wires ( $X_b = 0$ ), Eq. (4.3) will be simplified to

$$\mathbf{H} = H_z \hat{\mathbf{z}} = \frac{I_{mag} X_w}{\pi(X_w^2 + Z_b^2)} \hat{\mathbf{z}} \quad (4.8)$$

When  $X_w = Z_b$ , the magnetizing field at the bead center in Eq. (4.8) reaches its maximum

$$H_{z,max} = \frac{I_{mag}}{2\pi Z_b} \quad (4.9)$$

The analysis above shows that the distance between the two wires should be designed as approximately twice of the distance between bead center and wire center. For instance, with the sensor parameters shown in Figure 4-3, to maximize the magnetizing field for a 4.5- $\mu\text{m}$  bead, the distance between the wires should be around 6  $\mu\text{m}$ .

For the experiments in this dissertation, the current through the wires is chosen as 32 mA by considering the weak magnetizing field requirements for the bead susceptibility and relaxation given by Eq. (2.5) and Eq. (3.3), Joule heating of sensor surface [28], on-chip and off-chip voltage drops and electro-migration rules. With  $I_{mag} = 32$  mA and  $X_w = 3$   $\mu\text{m}$ , the magnetizing field at a M-450 bead center is 1.5 kA/m (1.9 mT). With the same wires, the magnetizing field is 2 kA/m (2.5 mT) for a M-280 bead and 2.6 kA/m (3.3 mT) for a MyOne bead.

The magnetic dipole moment of the bead  $\mathbf{m}$  can be expressed as

$$\mathbf{m} = \chi V_b \mathbf{H} \quad (4.10)$$

where  $V_b$  is the bead volume. With the susceptibility values calculated in Chapter 2, the magnetic moment of a M-450 bead is estimated to be  $\sim 110\text{f Am}^2$  whereas for M-280 and MyOne bead, the magnetic moments are  $\sim 18\text{f Am}^2$  and  $2.2\text{f Am}^2$  respectively.

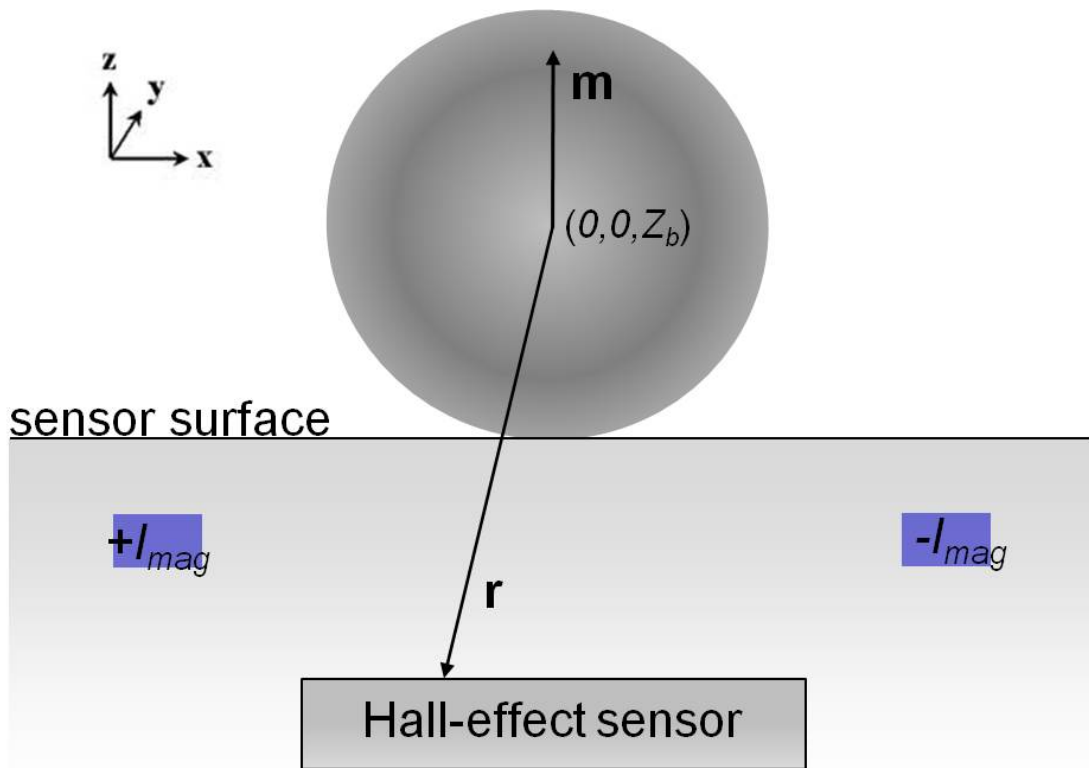


Figure 4-5: Calculation of the induced magnetic field from a bead to the underlying sensor.  $\mathbf{m}$  is the magnetic moment of the bead which is modeled as a dipole located at the bead center and  $\mathbf{r}$  is a vector pointing from bead center to the sensor.

For a small bead (e.g. MyOne bead) whose radius is much smaller than the distance from sensor center to chip surface ( $3 \mu\text{m}$  as shown in Figure 4-3), the bead can be modeled as a magnetic dipole located at bead center with magnetic moment  $\mathbf{m}$  (Figure 4-5). The induced field at the sensor is given by

$$\mathbf{B}(\mathbf{r}) = \frac{\mu_0}{4\pi} \frac{3(\mathbf{m} \cdot \mathbf{r})\mathbf{r} - \mathbf{m}r^2}{r^5} \quad (4.11)$$

where  $\mu_0$  is the vacuum permeability and  $\mathbf{r}$  is a vector pointing from the center of the bead to the point where the field is being measured. Since the bias current flows in x-direction in the Hall-effect sensor, the Hall voltage is only sensitive to magnetic field in

the z-direction  $B_z$ . Based on the magnetic moment calculated earlier, the maximum  $B_z$  induced by a MyOne bead at the center of an underlying Hall-effect sensor is about 10  $\mu\text{T}$ .

For a M-450 or M-280 bead, similar calculation shows the maximum induced  $B_z$  is  $\sim 160 \mu\text{T}$  (M-450) and  $42 \mu\text{T}$  (M-280), respectively. Since the bead radius is not negligible compared to the distance from sensor to chip surface, these values are about 30% less than finite-element analysis; however, since the calculation underestimates the induced field, it is still useful for a quick first-order analysis.

Due to the finite size of the Hall-effect sensor and the decaying signal, the measured bead relaxation signal is about five times smaller than the values given earlier. Such a small magnetic signal brings multiple challenges in the bead detection.

First, since the magnetic signal from single microbead is only tens of  $\mu\text{T}$  or even less, care must be taken to reject interferences from Earth's magnetic field ( $\sim 50 \mu\text{T}$ ), time-varying stray magnetic fields from power lines and nearby electrical equipment, and other urban noise.

Second, the DC offset from the Hall-effect sensors and the CMOS readout circuit is several orders-of-magnitude larger than the signal. The dominant offset arises from the miniaturized Hall-effect sensors due to fabrication imperfections such as contact misalignment [27]. The equivalent input-referred sensor offset was measured to be as large as 300 mT in a test chip previously developed in the same CMOS process, translating into a requirement of more than 90 dB DC offset rejection.

Additionally, thermo-electric and thermo-magnetic effects on the chip also introduce errors that significantly exceed the small signal from the bead. For instance, the thermopower of silicon is about 0.5 mV/K [29], or equivalently, 8.3 mT/K for the Hall-effect sensors presented here. So a local thermal gradient as little as one Kelvin can result in an error that is three orders-of-magnitude larger than the bead signal. To reduce the thermal effects, active sensors are surrounded by dummy sensors and the wires extend well beyond the sensor area to make the heat distribution more uniform along the sensors. However, the thermal gradient between the sensing contacts still generates a significant error compared to the signal. For sensors that are close to the edge of the array, this error is measured to be as large as 1.2 mT, almost two orders of magnitude larger than the bead signal.

Finally, flicker noise from the CMOS electronics and thermal noise from both the sensor and readout circuit must be considered.

## 4.4 Solutions

Several techniques are applied to reduce the errors discussed in the previous section.

First, the current through the wires is modulated. Therefore the bead signal is frequency-domain separated from the low-frequency errors such as DC offset, stray fields and flicker noise. The principle is illustrated in Figure 4-6. There are four phases in one modulation cycle. In phase 1, the bead is magnetized for  $t_m$  with the magnetizing field  $B_{mag}$ . The bead responds with its own magnetic field,  $B_{bead}$ . In phase 2,  $B_{mag}$  is removed rapidly and  $B_{bead}$  decays during  $t_r$  with a time constant described by Eq. (3.7). In phase 3, the magnetizing field is reversed and relaxation occurs again in phase 4. These four phases repeat for many cycles. The bead signal is thus modulated to frequency  $f_0 = \frac{1}{2(t_m+t_r)}$ . DC offset is then attenuated by a mixed-signal servo loop to be discussed in the next chapter and a signal processing technique described later in this section.

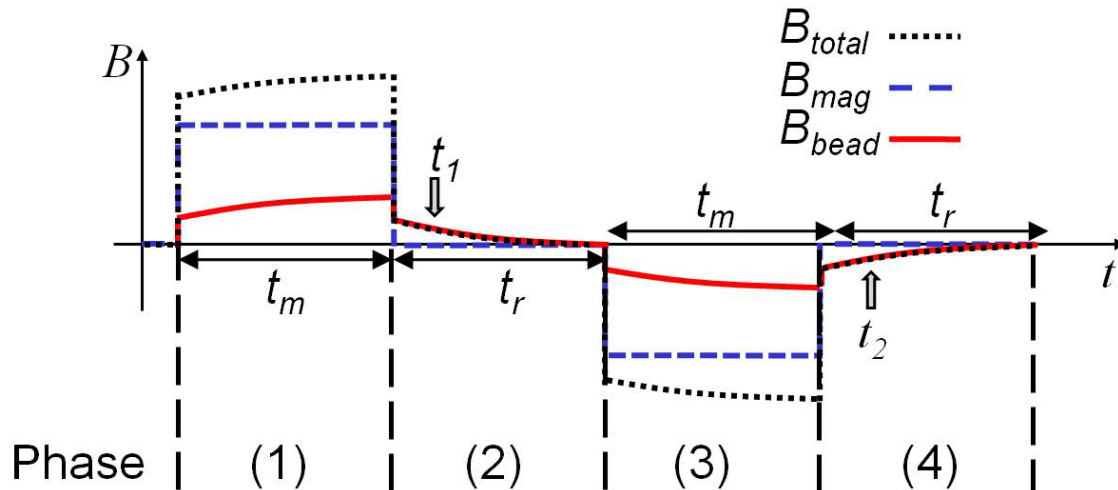


Figure 4-6: Magnetizing field modulation timing diagram

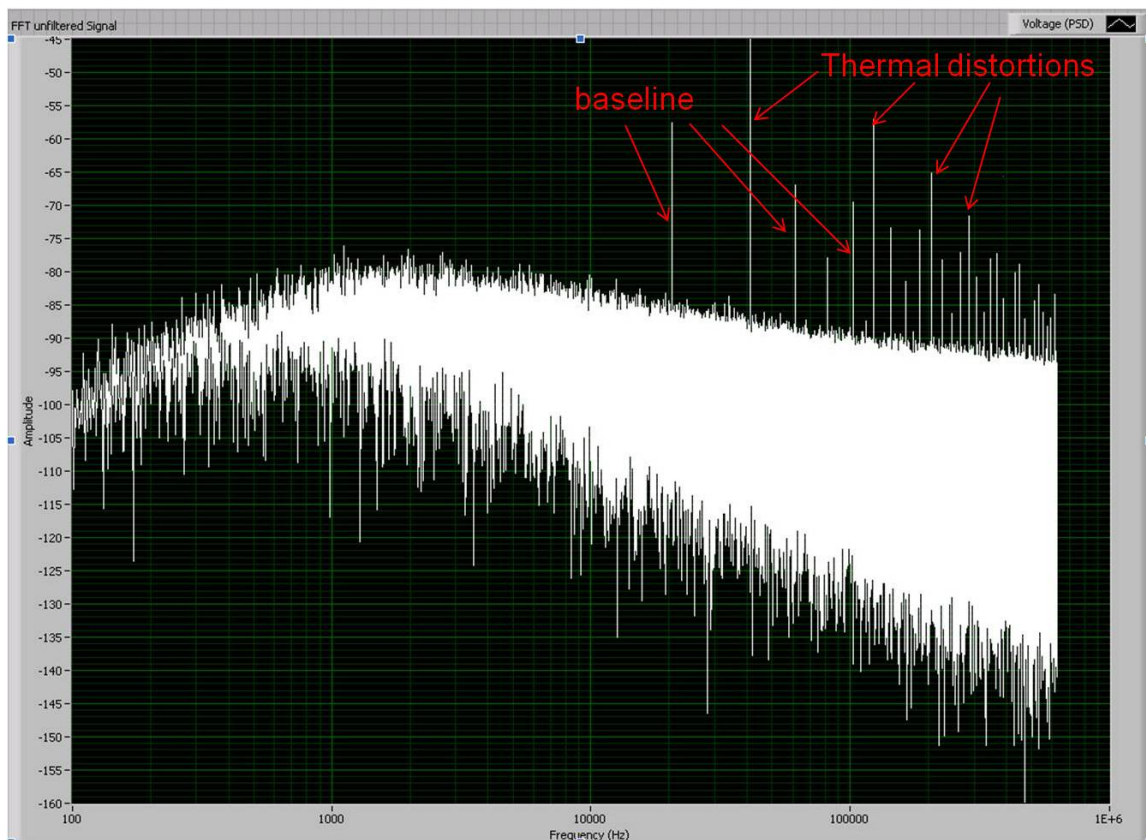


Figure 4-7: Spectrum of a sensor output after field modulation. No low-frequency non-idealities are shown here due to a high-pass RC filter (1 kHz cutoff frequency) in the measurement path. Flicker noise corner is about 50 kHz.

A typical sensor response with modulation is shown in Figure 4-7. Modulation frequency used here is 20 kHz. Baseline appears as odd harmonics. Bead signal, which is more than 40 dB lower than baseline, is overwhelmed by flicker noise and second harmonic distortion. The second harmonic distortion and its harmonics are caused by thermal effects, due to the fact that in each modulation cycle the current through a wire is turned on/off twice and thus the sensor goes through two heating/cooling cycles. Therefore flicker noise and thermal distortions must be attenuated before the bead relaxation is reconstructed.

Correlated double sampling (CDS) is applied to reject the thermal distortions and the low-frequency non-idealities. The net relaxation signal is measured by taking the difference between phases 2 and 4, and then averaging it over many cycles to reduce thermal noise. CDS can be easily understood in the frequency domain with the following transfer function

$$|H(f)| = |1 - e^{-j2\pi f(t_m + t_r)}| = 2 \sin\left(\frac{\pi f}{2f_0}\right) \quad (4.12)$$

which is plotted in Figure 4-8. Both second harmonics caused by thermal effects and low-frequency non-idealities (including stray field, flicker noise and DC offset) are attenuated by CDS [30]. After field modulation and CDS, the relaxation waveform initially overwhelmed by both offset and thermal distortions is reconstructed (Figure 4-9).

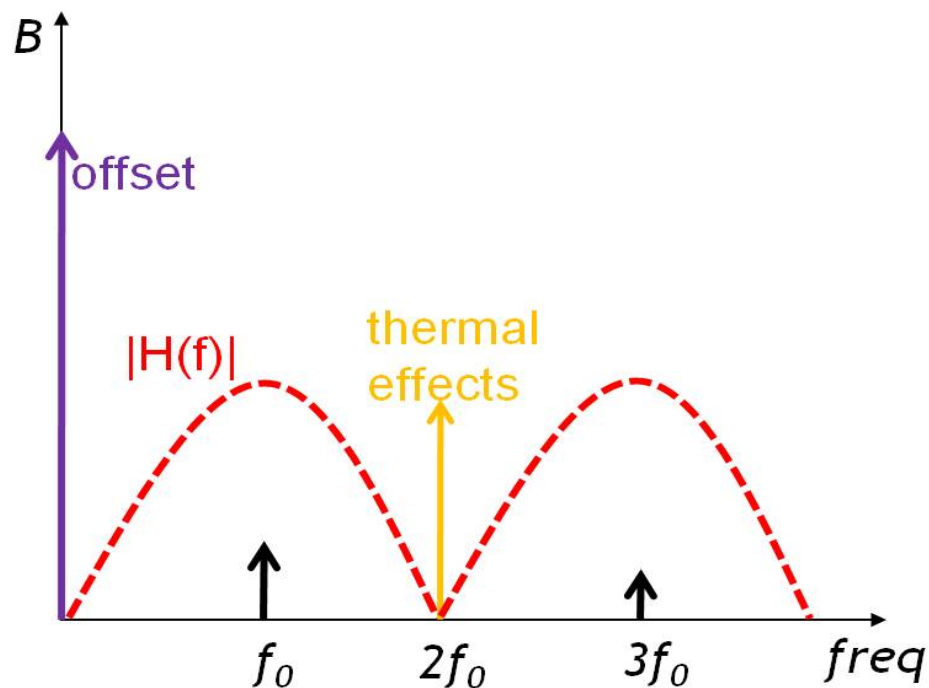


Figure 4-8: Suppression of DC offset and thermal effects by CDS (not to scale).

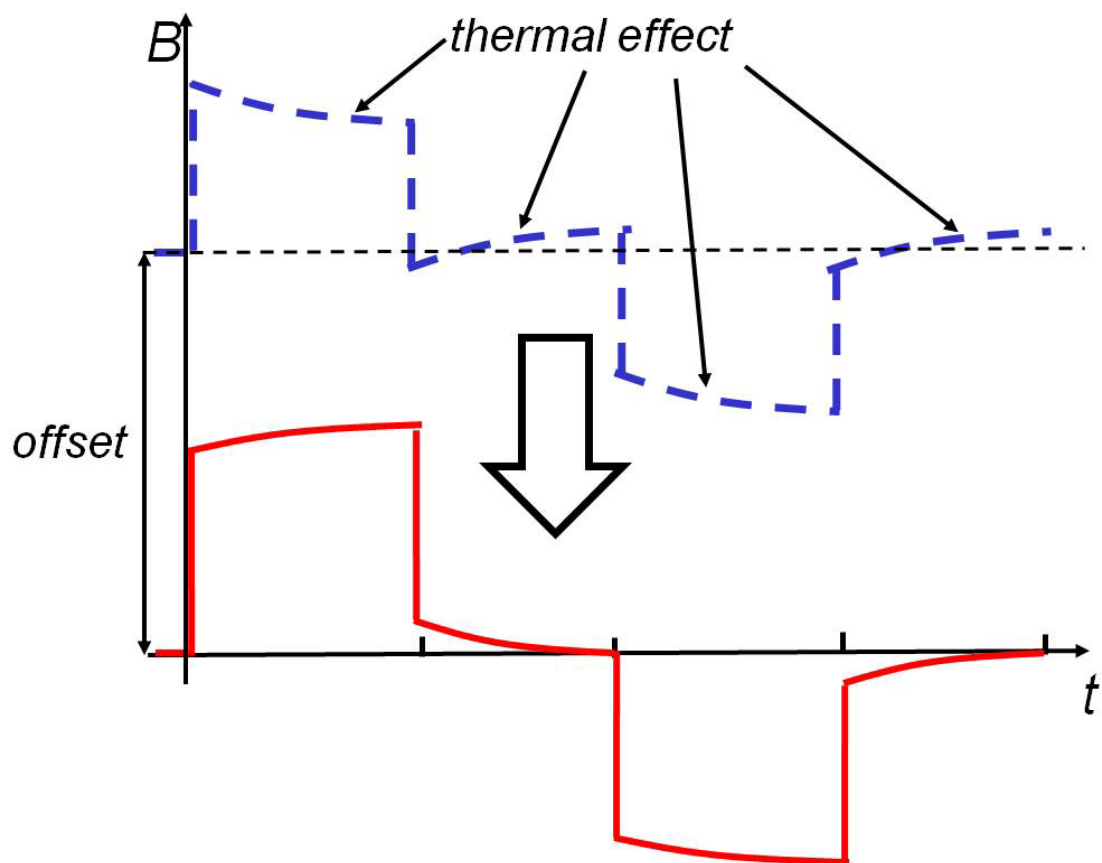


Figure 4-9: Reconstruction of signal with modulation and CDS (not to scale). Top: Modulated signal is distorted by DC offset and thermal effect. Bottom: DC offset and thermal effects removed by CDS.

## 4.5 Summary

CMOS Hall-effect sensors are amenable to integration but the voltage-related sensitivity is low in silicon. Post-processing is required to bring sensor surface close to the embedded Hall-effect sensor to increase bead signal strength; however, the magnetizing field is limited by weak magnetizing field requirements, Joule heating, voltage drop in the wires and electro-migration rules. The induced magnetic field from a microbead is about only 10  $\mu\text{T}$ .

Due to the small magnitude of the bead signal, non-idealities such as stray magnetic field, DC offset and thermal effects must be suppressed. Modulation of the magnetizing field and correlated double sampling are effective in rejecting low-frequency errors and thermal effects. DC offset is also attenuated through a mixed-signal servo loop to be discussed in the next chapter. Thermal noise is suppressed by data averaging. The challenges and solutions are summarized in Table 4-1.

Table 4-1: Summary of Design Challenges and Solutions

Challenges	Solutions			
	Relaxation	CDS	Mixed-signal loop	Data averaging
Large baseline	<b>X</b>			
Large sensor offset		<b>X</b>	<b>X</b>	
Large stray magnetic fields		<b>X</b>	<b>X</b>	
Sensor nonlinear effects		<b>X</b>		
Flicker noise		<b>X</b>		
Thermal noise				<b>X</b>

## Chapter 5

# System and Circuit Design

In this chapter, we will describe the design of a fully integrated magnetic bead detector based on magnetic relaxation. System level architecture is first discussed, followed by detailed design considerations and circuit implementation on the three building blocks: magnetic sensor, magnetizing field generator and readout channel.

### 5.1 System Architecture

A CMOS bead detector is designed to explore the relaxation of microbeads. Design parameters in the three building blocks are determined by trade-offs of signal-to-noise ratio, detection time and power consumption.

Since the magnetizing field does not need to be homogenous for the relaxation detection method, it can be generated on chip with appropriate wiring. The modulation frequency and field strength is determined based on the analysis of bead properties in Chapter 2 and Chapter 3. Aligning the magnetizing field with the sensitive axis of the detector increases the detector output, thus permitting the use of Hall-effect sensors available in standard CMOS technology and eliminating the need for non-standard magnetometers such as GMRs. The micron-sized beads generate only a localized field and cannot be detected by a single sensor with large area, so the magnetic sensor is organized into arrays. This array configuration, together with the relaxation detection method, significantly reduces the dynamic range and linearity requirement on the system level.



## 5.2 Hall-effect Sensor Element and Array

As discussed in the previous chapter, N-Well Hall-effect sensors are implemented in this prototype due to their higher carrier mobility and therefore higher sensitivity. The Hall plate size is optimized based on bead size, signal magnitude and physical design rules. According to Eq. (4.11), bead signal decreases with the third power of distance  $|\mathbf{r}|$ , so Hall plate size should be minimal to maximize bead signal. On the other hand, Eq. (4.1) is only valid for a thin Hall plate with small sense contacts. Therefore the lateral dimensions of individual Hall plate must be large compared to the sensing contacts and depth of the N-Well. Note the sensing contact referred here is the high-doping active region next to the N-Well, not the metal contact. In the 0.18- $\mu\text{m}$  CMOS technology used in this project, the minimum size of a sense contact is 0.45  $\mu\text{m}$ , whereas the depth of the N-Well is about 1  $\mu\text{m}$ . Therefore in this design, the width and length of the Hall plate are chosen to be 4  $\mu\text{m}$ .

The induced field from a bead to any point on the sensor can be calculated with Eq. (4.3) and Eq. (4.11). For instance, when a 1- $\mu\text{m}$  MyOne bead is located over the center of a 4- $\mu\text{m}$ -by-4- $\mu\text{m}$  sensor and magnetized by 32-mA current through wires 6  $\mu\text{m}$  apart, the peak induced field is about 10  $\mu\text{T}$  and the average field across the sensor is about 5.5  $\mu\text{T}$  (Figure 5-2).

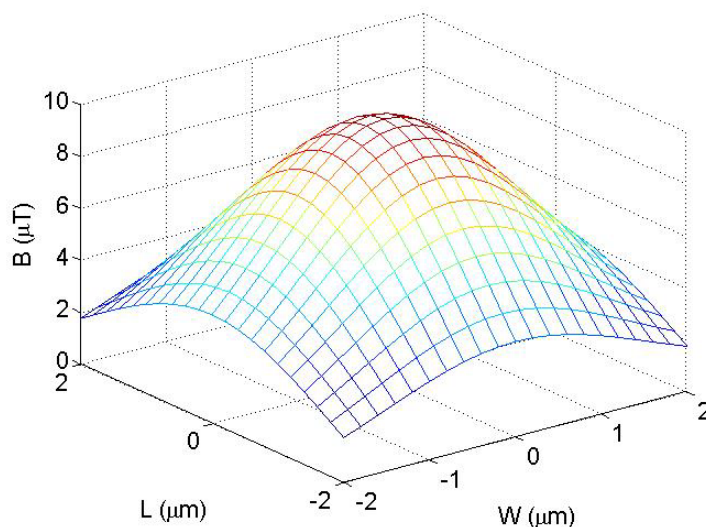


Figure 5-2: Induced field from a MyOne bead on a 4- $\mu\text{m}$  by 4- $\mu\text{m}$  Hall-effect sensor. Magnetizing current is 32 mA. The distance between the magnetizing wires is 6  $\mu\text{m}$ .

Each sensor element consists of two access transistors and a Hall plate (Figure 5-3). The Hall plate is represented by a four-terminal multiplier where the output (Hall voltage) is proportional to the input (bias voltage) as given by Eq. (4.1). The sensor element resembles a 6-T SRAM cell from an architecture perspective. In each sensor element, there are two access transistors ( $M_0$ ,  $M_1$ ) which are controlled by word line ( $WL$ ). The Hall voltage signal is carried by bit lines ( $V^+$ ,  $V^-$ ). The Hall plate is connected between  $V_{bias}^+$  and  $V_{bias}^-$  with a bias voltage around 2 V.

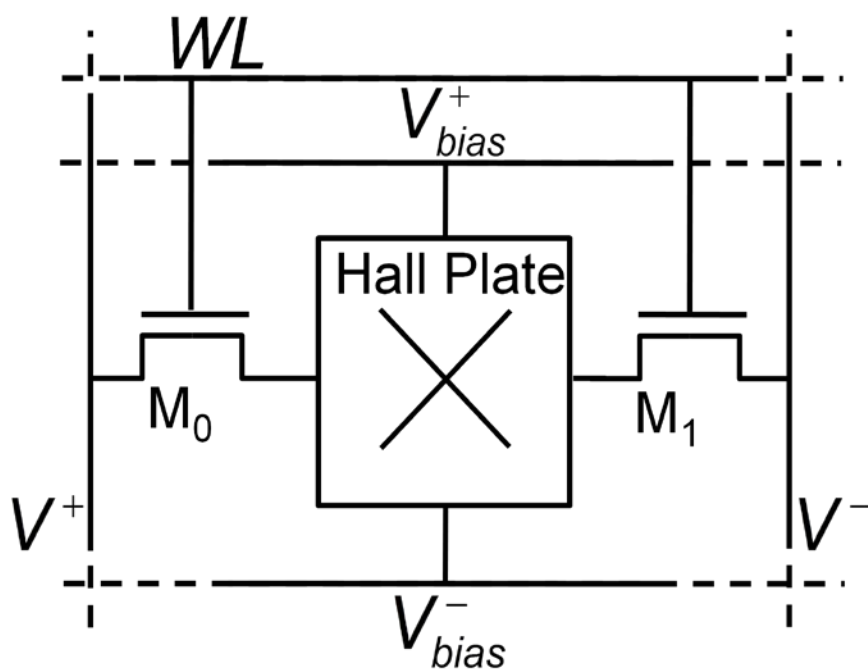


Figure 5-3: Sensor element schematic

For simulation, a heuristic AC model for Hall plate can be used [27]. For MHz modulation with high output (sensing) impedance, the model can be simplified as shown in Figure 5-4. The resistors  $R_{H0} \sim R_{H3}$  are the resistance between the terminals of a Hall plate. The Hall plate offset can be represented by a mismatch in the resistor bridge. For an ideal Hall plate, the resistors are all identical so there is no offset. The resistance can be estimated with Hall plate dimensions and sheet resistance of N-Well under STI.  $E_0 - E_3$  are voltage controlled voltage source to model the Hall voltage signal, which is given by

$$E = \frac{S_V(V_{bias}^+ - V_{bias}^-)B}{2} \quad (5.1)$$

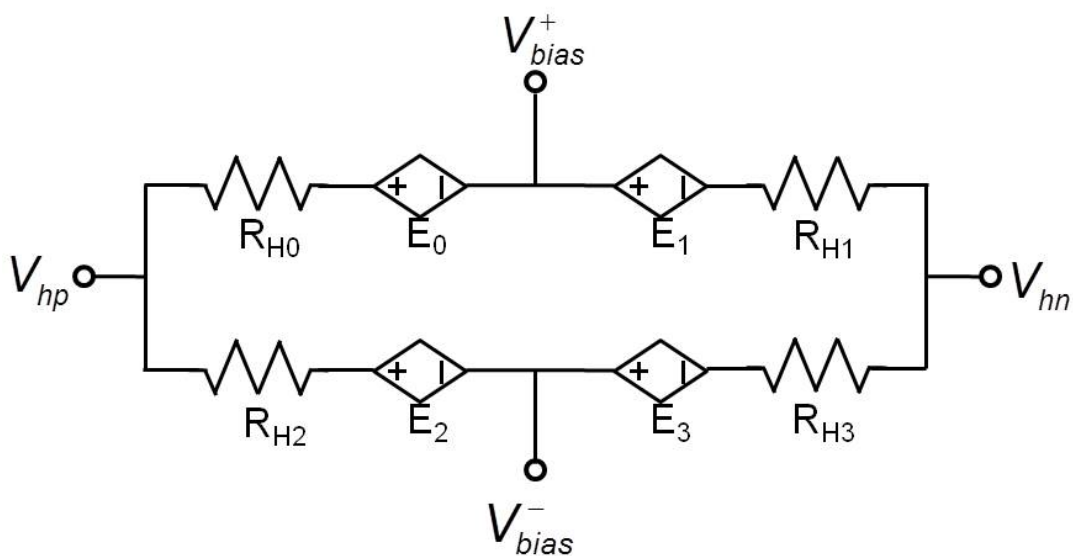


Figure 5-4: Simplified Hall plate model

As described earlier, the post-processing steps limit the available interconnects to metal one and polysilicon only. Metal is routed horizontally and used for the wires that carry 32-mA alternating current  $I_{mag}$ , sensor bias  $V_{bias}$ , and the row select signal  $WL$  (Figure 5-5). The Hall voltages  $V^+$  and  $V^-$  (“bit lines”) are partially routed in polysilicon, which results in parasitic resistance that must be considered for large array.

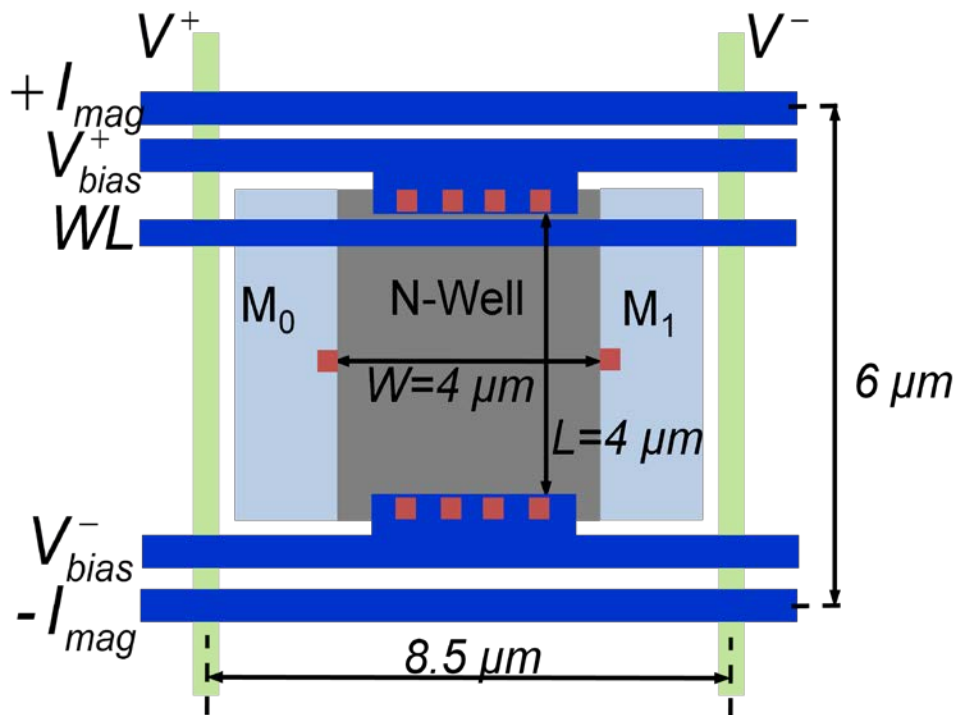


Figure 5-5: Layout of a sensor element. Sensing contacts are defined by N+ doping. Metal one layer runs horizontally for magnetizing, sensor bias and row selection. Polysilicon is used for signal output routing. Each sensor element occupies  $8.5 \mu\text{m} \times 6 \mu\text{m}$ .

For N-Well Hall-effect sensors, the bias current flows in the substrate rather than along the surface. Therefore the flicker noise is negligible and not considered here. The total noise from a sensor includes the thermal noise from Hall plate, access transistors and bit line parasitic resistance (Figure 5-6). For sensor array with  $N$  rows, the total noise contributed by sensor is given by

$$\frac{\overline{v_{i,hall}^2}}{\Delta f} = 4kT(R_{out} + R_{eq0} + R_{eq1} + 2NR_{bl,cell}) \quad (5.1)$$

where  $R_{out}$  is the output resistance of the Hall plate between the sensing contacts.  $R_{eq0}$  and  $R_{eq1}$  are the equivalent on-resistance of access transistors M0 and M1, respectively.  $R_{bl,cell}$  is poly resistance on bit line in each cell.

For small contacts,  $R_{out}$  can be estimated by [27]

$$R_{out} \approx \frac{2R_{\square}}{\pi} \ln\left(\frac{W}{S}\right) \quad (5.2)$$

where  $R_{\square}$  is the sheet resistance of N-Well under STI,  $W$  and  $S$  are the width of Hall plate and sense contact respectively. With the parameters in the CMOS technology used here,  $R_{out}$  is estimated to be 1275  $\Omega$ .

To make the sensor noise dominated by Hall plate, the access transistors and bit lines must be wide enough. On the other hand, although the stray field from beads landing between sensor elements can be detected by adjacent Hall plates, excessive gaps necessitated by larger access transistors and bit lines would result in reduced signal-to-noise ratio and consequent increased detection error or measurement time. Therefore the access transistors are optimized to be 3.2/0.18  $\mu\text{m}$  so that  $R_{eq0,1}$  is around 440  $\Omega$ . Each access transistor is implemented with four fingers to minimize sensor width.  $R_{bl,cell}$  is about 19  $\Omega$  in the final design. In this prototype, only 16 rows of sensors are implemented, so in the worst-case scenario the parasitic resistance on the bit lines is 608  $\Omega$ , which still contributes less noise than Hall plate and access transistors. Typical thermal noise from a sensor element is about 97 nT/Hz<sup>1/2</sup> at room temperature.

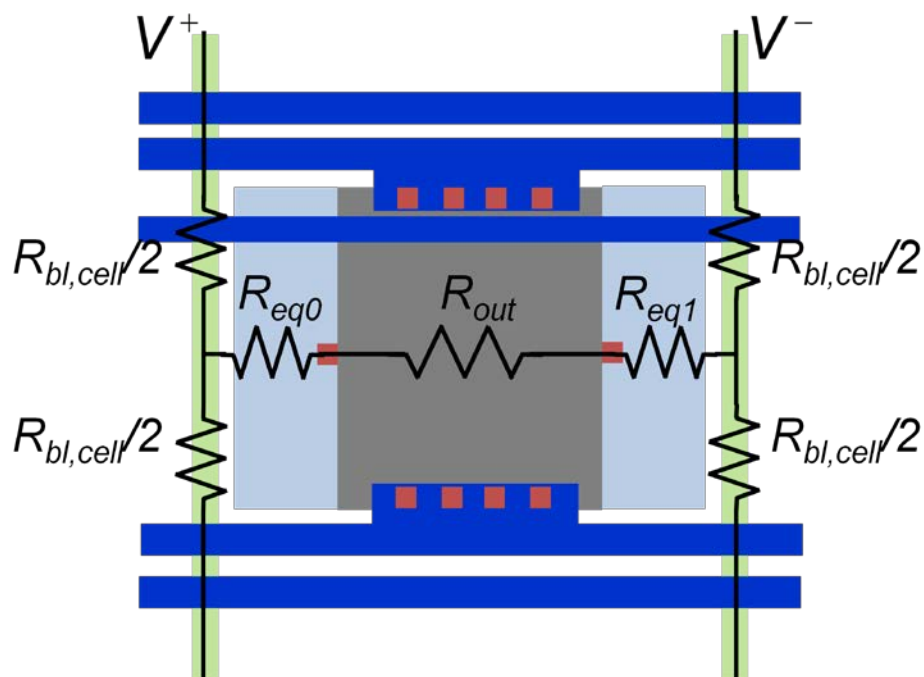


Figure 5-6: Noise model of a sensor element

Similar to cells in SRAM array, in a Hall-effect sensor array a word line is shared by sensors in the same row whereas bit lines connect sensors in columns (Figure 5-7). Since the Hall plate is resistive, switches must be added to the bias line in order to turn on only one row of sensors each time. For a row with 8 sensors, the resistance between  $V_{bias}^+$  and  $V_{bias}^-$  is less than  $120\ \Omega$  so the bias switches must be wide in order to make the voltage drop negligible. In addition, the parasitic resistance on  $V_{bias}^+$  and  $V_{bias}^-$  lines must be considered to minimize bias voltage variation among sensor elements.

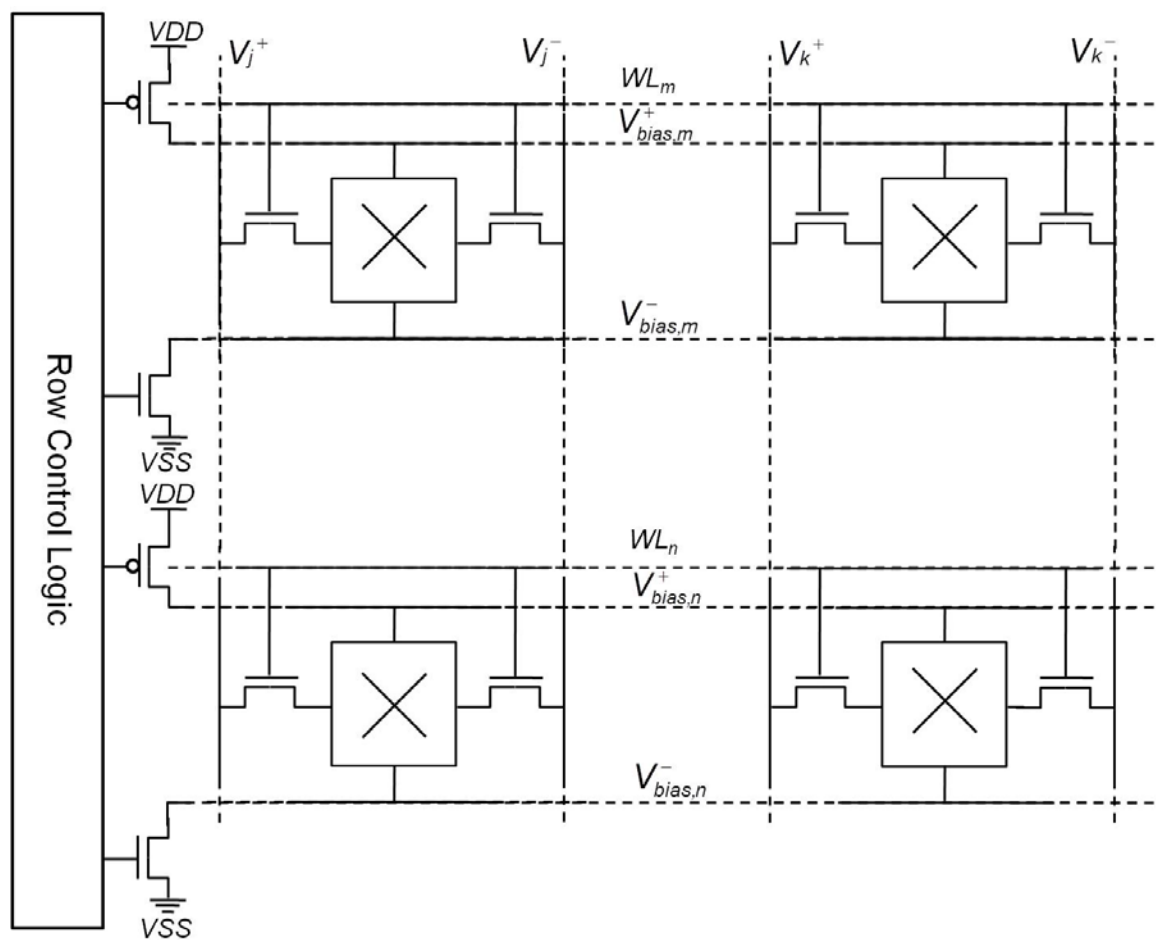


Figure 5-7: Sensor array schematic. Two bias switches are added in each row.

The array layout is critical in minimizing the parasitic resistance while keeping high packing density (Figure 5-8). Magnetizing wires are shared by adjacent rows of sensors. Each bias switch is split into two and located on the left and right side of the sensor array. The sensor bias lines are only  $0.6\text{-}\mu\text{m}$  wide but carry as much as 16 mA for a row of 8 sensors. To reduce IR drop in the bias lines, those of adjacent rows are connected with poly so the parasitic resistance almost by half. With a 2-V power supply, the sensor elements consume an average of 2.1 mA with less than 2% variation among sensors.

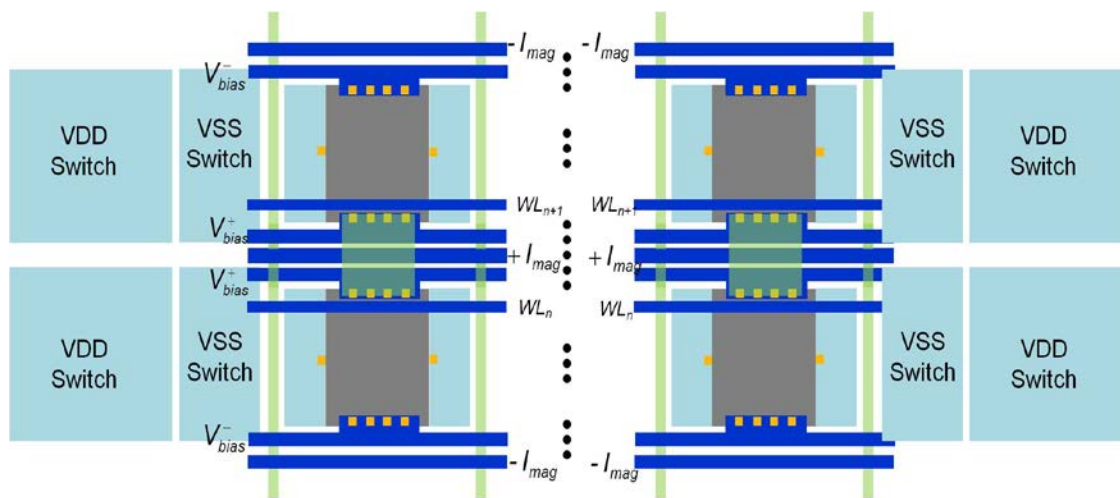


Figure 5-8: Sensor array layout. Sensor switches are located on two sides of the sensor array. Sensor bias lines of adjacent rows are connected to reduce voltage drop.

The micrograph of an 8x8 array is shown in Figure 5-9. Dummy sensors and bias switches are not shown here. For a magnetic bead assay, it is important to have a large detection area to reduce the measurement uncertainty [31]. Two adjacent rows of sensors share one wire to increase packing density and thus maximize signal amplitude. The worst case occurs when a bead lands between two sensors and the signal is attenuated by about 50% based on simulation [23, 32] and experiment [33].

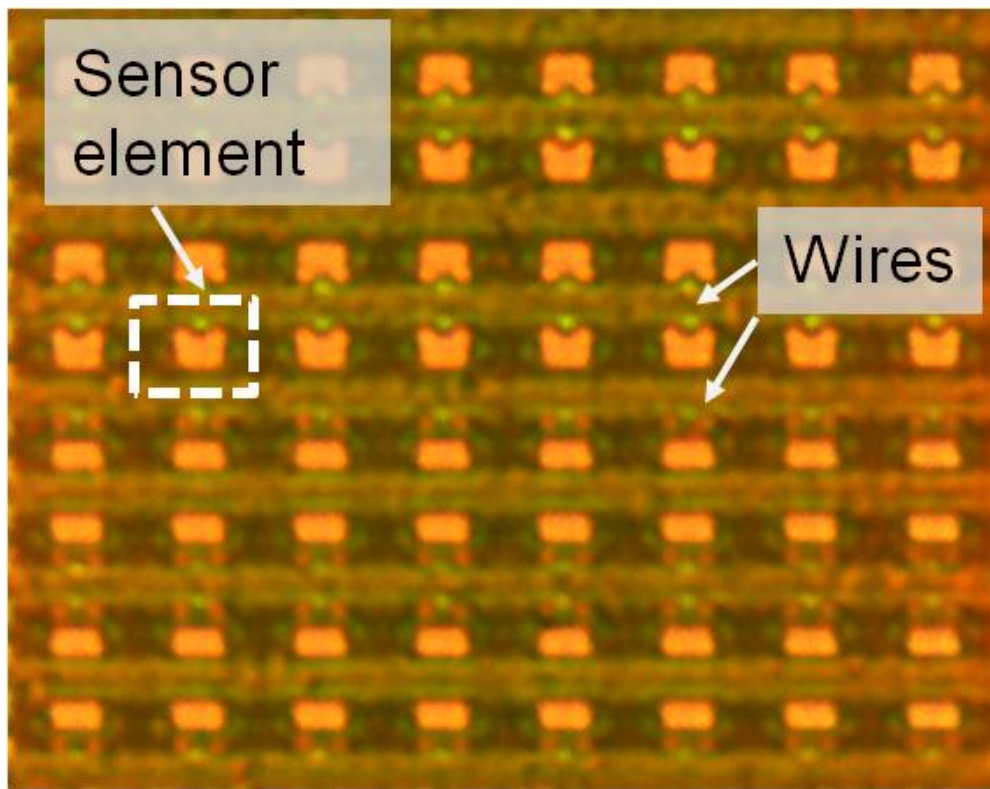


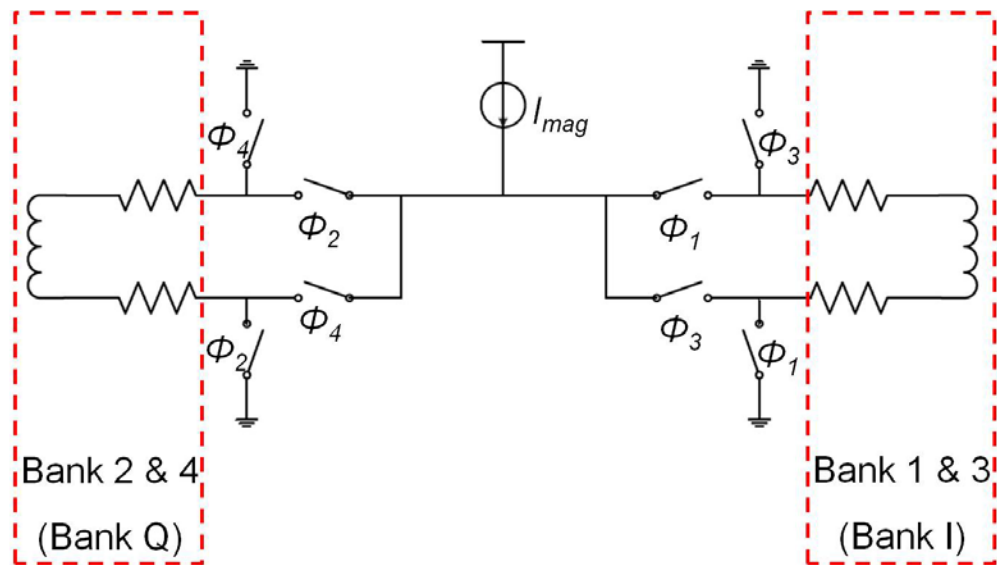
Figure 5-9: Micrograph of an 8x8 sensor array

## 5.3 On-chip Electromagnet and Modulation

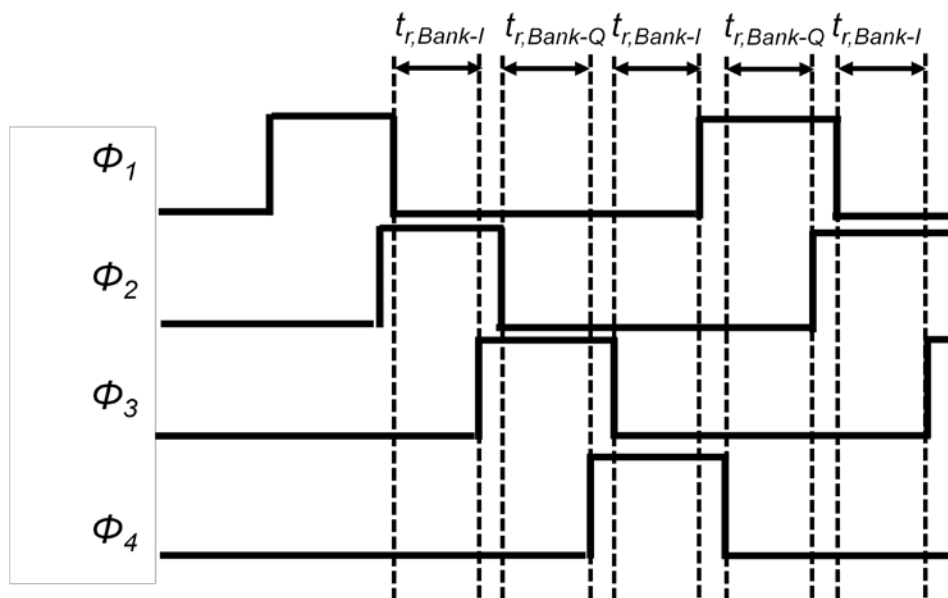
Thanks to the proximity to the bead and sensor, much smaller magnetizing fields are required, resulting in on-chip electromagnet implementation and significantly reduced power dissipation versus external magnet solution. Each row of sensors is magnetized by an electromagnet implemented with a pair of metal wires carrying a 32-mA current in opposite directions. As described in previous chapters, the magnetizing current is chosen by taking into account the weak-field requirement for bead, sensor surface temperature increase that might denature antibodies, IR drop and electromigration rules. For beads located at the center of sensor surface, the magnetizing field is 2.6 mT at the center of a M-280 bead and 1.8 mT for a M-450 bead, respectively. The average magnetizing field at the Hall plate (the “baseline”) is 2.9 mT.

Field modulation is implemented by alternating the current between different wires. The modulation frequency is controlled by a master clock of 64 MHz and is programmable from 1 kHz to 1 MHz with on-chip dividers, to magnetize MNPs of various sizes in a Dynabead and explore the shortest measurement time for the same SNR. Figure 5-10 shows the schematic of the switching network for one row of sensors in bank 1/3 and bank 2/4. The 32-mA magnetizing current is realized by an external 1-mA reference current and an on-chip 32x current mirror. Switches control the direction of the current and the bank where the current is routed. Make-before-break switching, realized by overlapping the switch control signals, keeps the total current constant, thus significantly reducing switching noise. While the total inductance ( $\sim 120$  pH) is negligible at the MHz modulation frequency, the total resistance of the switches and wires must be small so that the current source has sufficient head room to maintain a high output resistance. The resistance for each wire and switch is  $20 \Omega$  and  $4 \Omega$ , respectively. To maintain the magnetizing current constant during different phases, the current source is implemented with a cascode configuration to achieve over  $1\text{-k} \Omega$  output resistance and thus make the load resistance variation due to switch mismatches negligible.

The timing diagram of the switch network is shown in Figure 5-10b. Note the modulation causes in-phase and quadrature signal from bank 1/3 (bank I) and bank 2/4 (bank Q) respectively. When bank 1/3 is in magnetization phase, bank 2/4 is in relaxation phase and vice versa, enabling sharing of a readout channel and halving the time required to measure the entire array.



(a)



(b)

Figure 5-10: On-chip electromagnet. (a) Switch network for one row of sensors and (b) timing diagram of the switches.

## 5.4 Readout Channel

### 5.4.1 Offset Servo Loop

The error sources for offset and thermal noise at the input of the readout channel is shown in Figure 5-11. The offset is dominated by sensor offset  $v_{os,hall}$ , which is measured to be 97 mT (1- $\sigma$  value). Each gain stage adds extra offset  $v_{os,G1-4}$  due to MOS transistor mismatches.

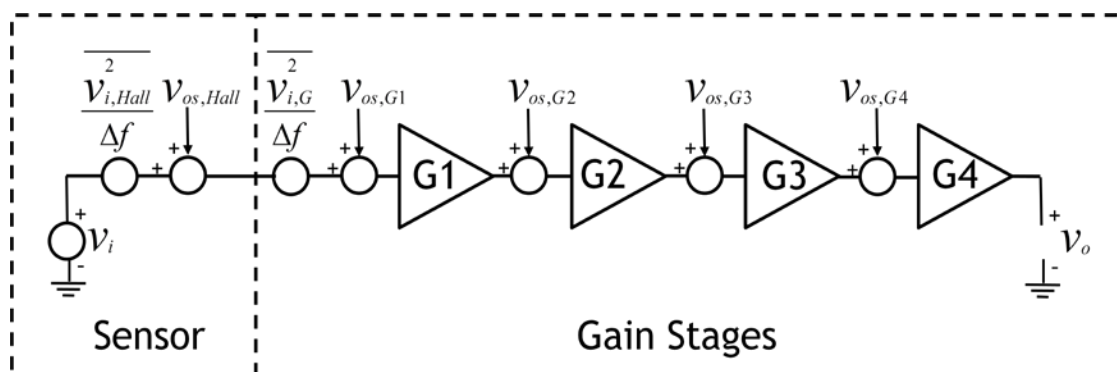


Figure 5-11: Offset and noise sources

As discussed in Chapter 4, the offset must be attenuated by more than 90 dB for signal detection. Although sensor offset can be rejected by AC coupling, it will result in a significant area or noise penalty. Conventional Hall-effect sensor offset-cancellation techniques such as spinning-current and pairing [27] could not be applied due to significant array area increase.

In our architecture, the offset cancellation is accomplished with the combination of an offset servo loop and CDS.

The offset cancellation in the servo loop is realized by 4-bit calibration DACs in each of the four programmable gain amplifiers (PGAs) that process the sensor output (Figure 5-12). The first PGA is designed to have a  $3\text{-}\sigma$  input-referred offset less than  $30\text{ mT}$  ( $\sim 1.7\text{ mV}$ ). Since the total input offset is dominated by the sensor, the offset cancellation starts sequentially from the first stage by binary search. The output of the G1 is first selected and the settings for its 4-bit DAC are determined after the calibration is complete for the first stage. The calibration continues for the second stage with both G1 and G2 in the servo loop. The servo loop then searches for G2 DAC setting that minimizes the offset. After the calibration is completed for all four stages, the equivalent input offset is reduced to less than  $27\text{ }\mu\text{T}$ , which is comparable to a microbead signal. This offset calibration can be performed anytime, even during bioassays when beads are immobilized on sensor surface, since the offset value is independent of applied magnetizing field. To minimize the offset drift, in our measurement, the calibration is performed right before a bead relaxation measurement.

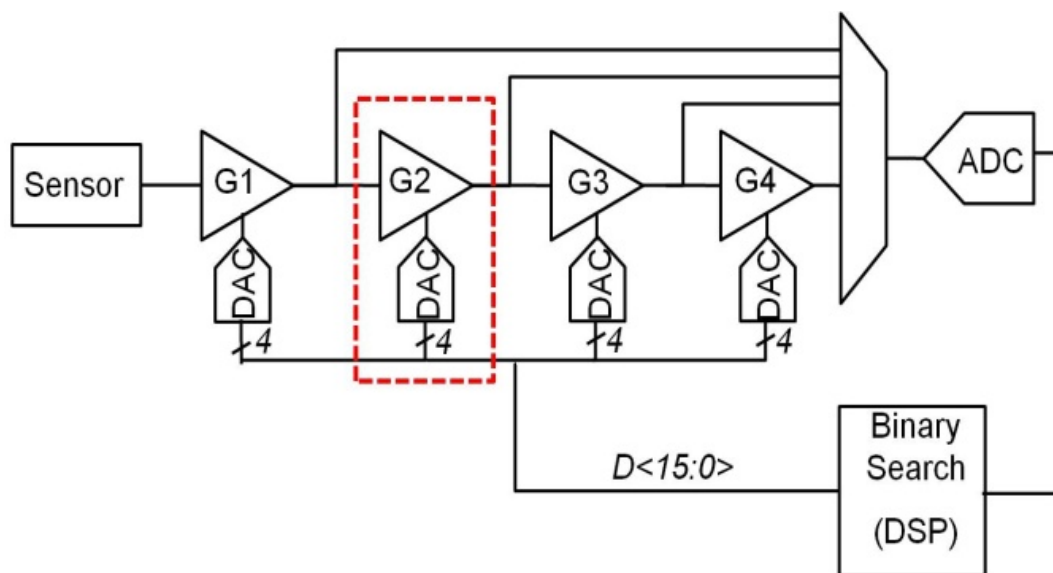


Figure 5-12: Block diagram of the mixed-signal loop for offset cancellation

The PGA output is sampled at 64 MS/s. Data is averaged for 0.5 ms for each binary search to reduce thermal noise. The entire offset cancellation process takes about 8 milliseconds. Offset cancellation is immediately followed by the relaxation measurement and the sequence is repeated for every sensor (Figure 5-13). The residue offset is further suppressed during the relaxation measurement by CDS. After CDS, the offset is sub- $\mu\text{T}$  and negligible compared to the bead relaxation signal. For this prototype, CDS is performed in the DSP.

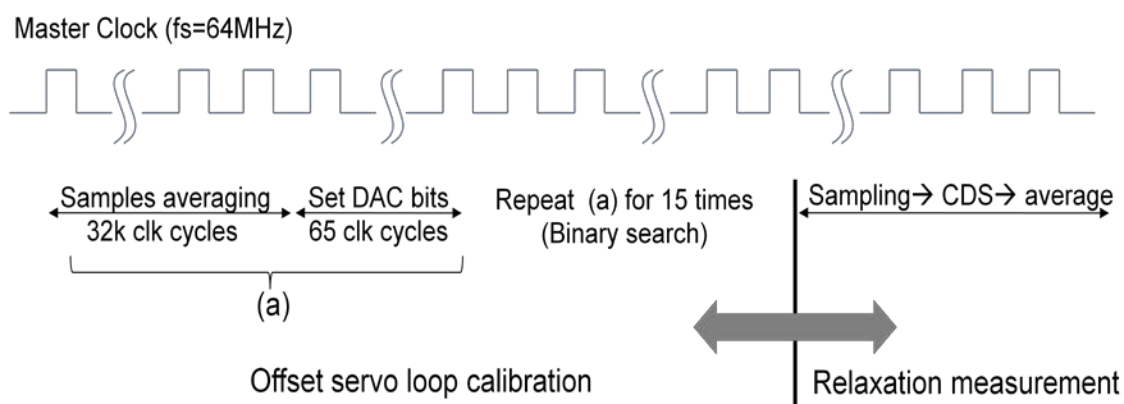


Figure 5-13: Timing diagram of sensor offset calibration and measurement

## 5.4.2 PGA and DAC

The schematic diagram of one PGA gain stage with a 4-bit DAC is shown in Figure 5-14. In each PGA, the DAC is designed to cancel a maximum input offset of  $\pm 300$  mT (18 mV). An open-loop gain stage and resistive loads are chosen for their low input-referred noise contribution. The input differential pair is implemented with PMOS transistors to reduce flicker noise. The transconductance of the first input stage is designed to be 4.4 mS so that thermal noise contribution from a readout channel is less than that of a sensor element. The noise contribution from DAC compared to that of the gain stage is given by

$$\frac{\overline{i_{n,DAC}^2}}{\overline{i_{n,amp}^2}} = \frac{4kTg_{m,DAC}}{4kTg_{m,amp}} = \frac{I_{DAC}/V_{DAC}^*}{I_{amp}/V_{amp}^*} \quad (5.3)$$

In this design  $V^*$  is chosen as 150 mV for both amplifier and DAC so Eq. (5.3) becomes

$$\frac{\overline{i_{n,DAC}^2}}{\overline{i_{n,amp}^2}} = \frac{I_{DAC}}{I_{amp}} = \frac{V_{OS}}{V^*} \quad (5.4)$$

When  $V_{OS} = 18$  mV and  $V^* = 150$  mV, Eq. (5.4) shows that the noise contribution from DAC is negligible compared to the gain stage. The total input-referred thermal noise of the readout electronics is  $73$  nT/Hz<sup>1/2</sup>.

Total current consumed by G1 is 720  $\mu$ A where 80  $\mu$ A goes to the DAC. Note in this prototype, since total power is dominated by sensors and magnetizing current, the readout channel is not optimized and each PGA consumes the same amount of power. The readout channel has a total power consumption of 6.2 mW and -3dB bandwidth of 10 MHz.

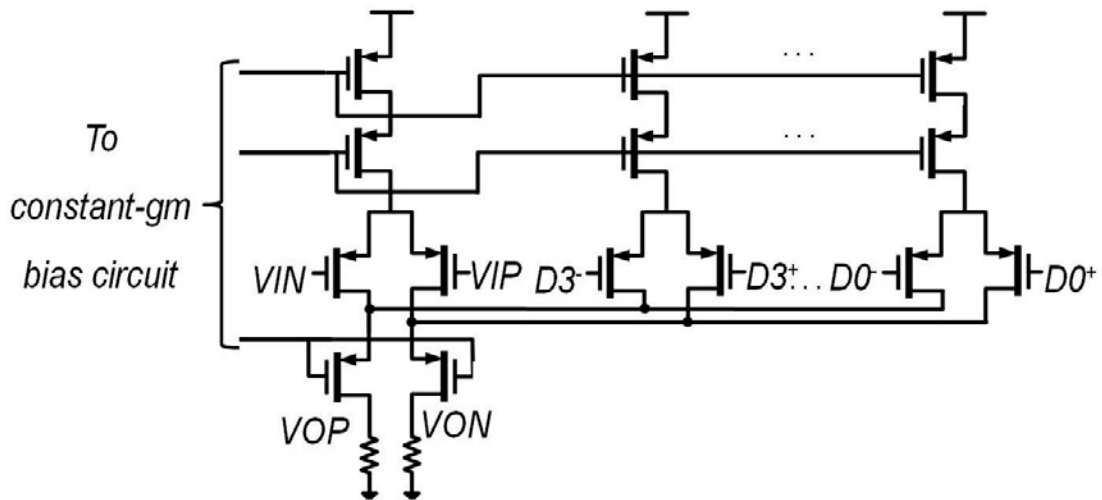


Figure 5-14: Schematic diagram of one gain stage and DAC

In each gain stage, cascoded transistors are used to isolate the output from input and minimize Miller capacitance. To control the gain variation, the PGA current is set by a constant- $g_m$  bias circuit (Figure 5-15). The transconductance of  $M_{b0}$  is given by

$$g_{m,M_{b0}} = \frac{2(1 - \sqrt{\frac{W_{b0}}{W_{b1}}})}{R_b} \quad (5.5)$$

where  $W_{b0}$  and  $W_{b1}$  are the widths of transistors  $M_{b0}$  and  $M_{b1}$ , respectively;  $R_b$  is the bias resistance. When  $W_{b0} = W_{b1}/4$ , Eq. (5.5) is simplified to

$$g_{m,M_{b0}} = \frac{1}{R_b} \quad (5.6)$$

By making the load resistance and the transconductance of the gain stage tracking  $R_b$  and  $g_{m,M_{b0}}$  in the bias circuit, the gain variation is less than 10% over PVT in simulation.

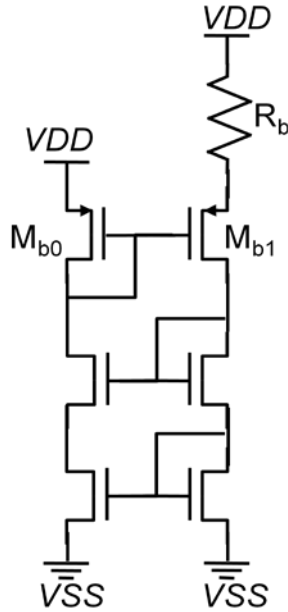


Figure 5-15: Schematic diagram of the constant-gm bias circuit

The gain of each of the first two stages is fixed at 20 dB. The last two stages are source degenerated with total gain programmable from 25dB to 37 dB in 6-dB steps. Each DAC is chosen to be 4-bit so that for every stage the total offset is within the DAC's range. The DNL and INL for binary-weighted DAC due to device mismatch are

$$\sigma_{DNL} \approx \sqrt{2^B - 1} \sigma_u \quad (5.7)$$

$$\sigma_{INL} \approx \frac{\sqrt{2^B}}{2} \sigma_u \quad (5.8)$$

where  $B$  is the number of DAC bits,  $\sigma_u$  is the coefficient of variation for unit current element given by

$$\sigma_u = \frac{\sigma_{th}/\sqrt{WL}}{V^*} \quad (5.9)$$

where  $\sigma_{th}$  the threshold voltage variation,  $W$  and  $L$  are the dimensions of the unit current source. With  $B = 4$ ,  $V^* = 150$  mV and  $\sigma_{th}$  given by the CMOS foundry, the 3- $\sigma$  DNL and INL in the final design are less than 0.1 LSB.

## 5.5 Discussion

The sensor element can be improved by circuit design techniques and technology change. For instance, the required size of access transistors can be reduced using word-line boosting [34]. Furthermore, since this chip is fabricated in a double-poly process, the sensor surface is farther from the Hall plate than in a single-poly process. Fabrication in a single-poly process would result in increased signal amplitude.

Unlike many other sensor devices, the Hall-effect sensor will also benefit from technology scaling. Reduced access transistors and Hall plate dimensions, enabled by scaled n-well thickness, smaller sensing contacts, and thinner metal and ILD, result in smaller sensor element and higher packing density. In fact, for the same induced bead field, the size of bead scales by roughly the same factor as technology. Assuming the technology scaling factor is  $\alpha$  and sensor array size stays the same, then the following statements hold true

- Magnetizing current scaled by  $\alpha$
- Bead-wire distance scaled by  $\alpha$
- Bead size is scaled  $\alpha$
- Bead-sensor distance  $r$  is scaled by  $\alpha$

Based on Eq. (4.9), (4.10), (4.11) and the statements above, we can also get

- Magnetizing field remains the same since both magnetizing current and bead-wire distance are scaled by  $\alpha$
- Bead magnetic moment  $m$  is scaled by  $\alpha^3$ .
- Induced field from the bead on the embedded sensor  $B_{bead}$  is constant since bead-sensor distance  $r$  is scaled by  $\alpha$  and  $B_{bead} \propto m/r^3$

Therefore in a more advanced technology node, smaller bead and less magnetizing current is required to generate the same induced field. For instance, the magnetic field induced by a 1- $\mu\text{m}$  bead measured by sensors implemented in 180-nm technology is roughly the same as the induced field by single 120-nm bead measured by sensors implemented in 22-nm process. Even though the Hall voltage output is about 2X smaller in 22-nm process due to power supply reduction, technology scaling stills plays significant role in detection limit improvement, sensor area reduction and chip power saving.

In this prototype, only one readout channel is implemented. For rapid detection, multiple channels could be implemented for parallel readouts. As the sensor array grows,

the sensors and readout channels will become the dominant source of chip power consumption. The power dissipated on sensing activity, however, could be drastically reduced with “sleep mode” control, where sensors and readout channels are only active during the relaxation measurement (Figure 5-16). Readout channels are shared between bank I and Q to save power and layout space. Since the bead signal decays during relaxation, the measurement interval could be shorter than the complete relaxation phase for a tradeoff between signal-to-noise ratio and power consumption.

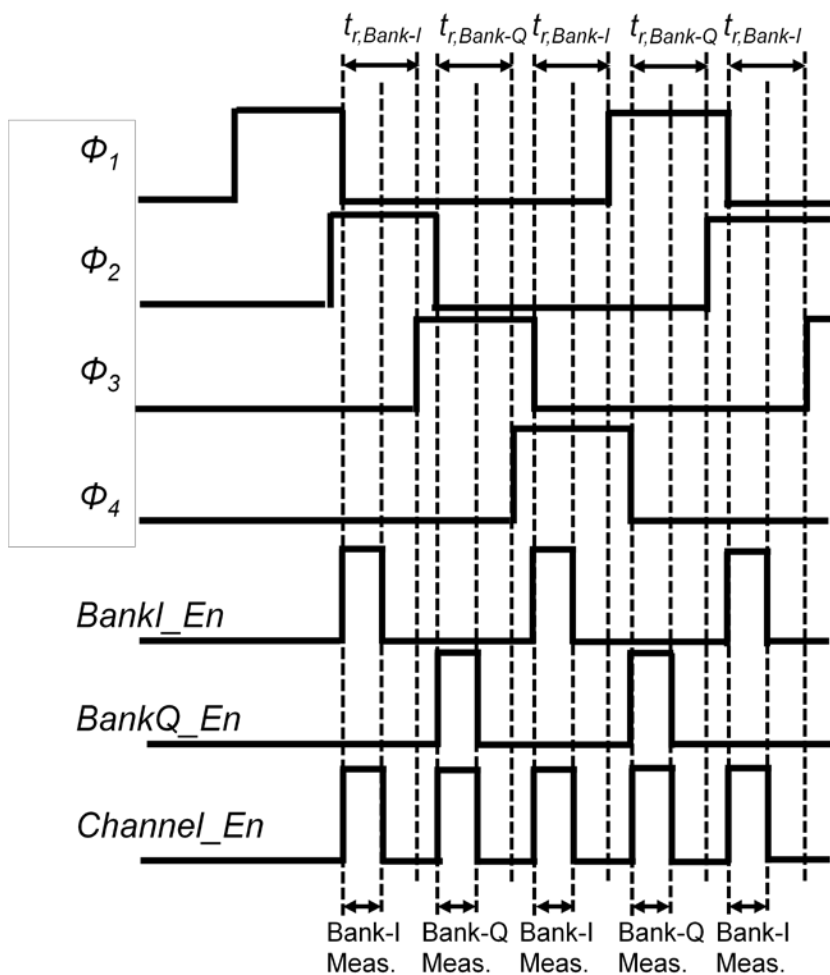


Figure 5-16: Sensor sleep mode for power saving

## 5.6 Chip Implementation

The microbead detector is implemented in 0.18  $\mu\text{m}$  CMOS. The die photo after post processing is shown in Figure 5-17. The sensor banks and electromagnetic modulation block (including the current source and switches) occupy  $650\ \mu\text{m} \times 235\ \mu\text{m}$ . The whole chip measures at  $2.5\ \text{mm} \times 2.5\ \text{mm}$ . To reduce substrate and power supply coupling, the digital block is kept at one corner of the chip with separate power supply. Both the analog and digital blocks operate with 2-V.

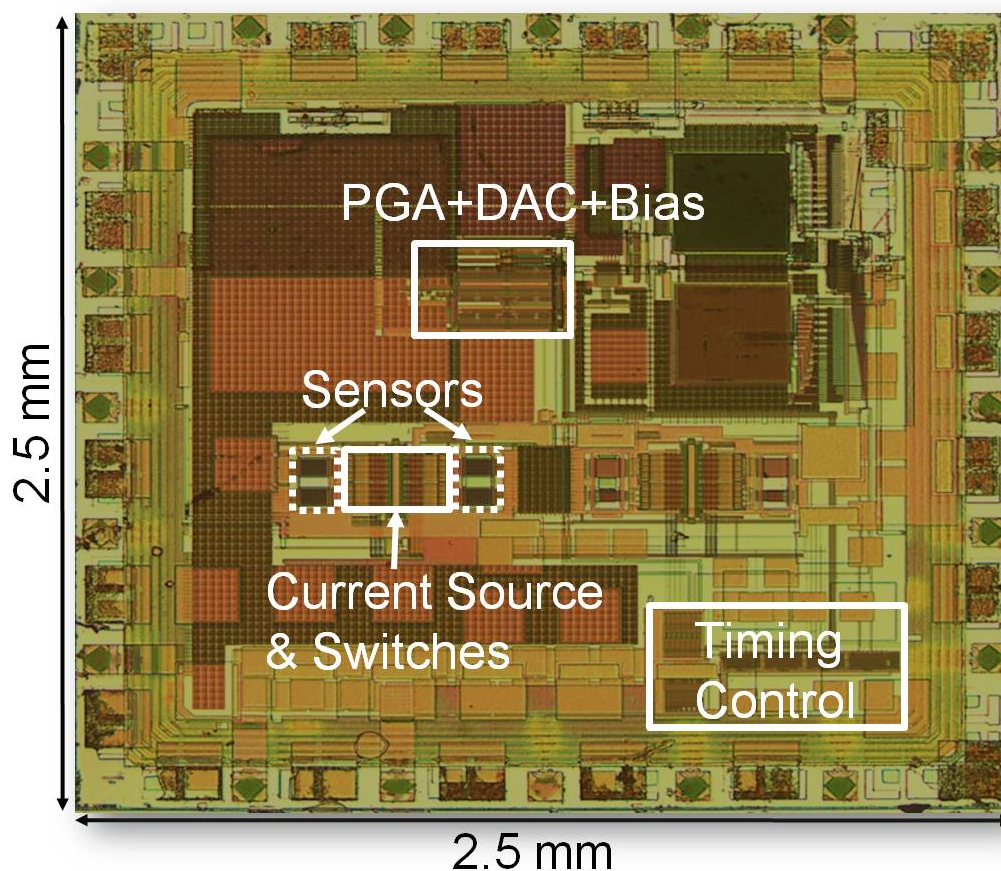


Figure 5-17: Die photo of the magnetic bead detector

## 5.7 Summary

A fully integrated magnetic bead detector based on magnetic relaxation is implemented in 0.18- $\mu\text{m}$  CMOS. Four banks of 64 active Hall-effect sensors are realized with each sensor element occupying  $8.5 \times 6 \mu\text{m}^2$ . Sensor element and array are optimized for high signal-to-noise ratio. Magnetic field modulation is achieved by precisely controlling a 32-mA current through on-chip metal wires. Sensor offset, as large as a few hundred mT, is suppressed to sub- $\mu\text{T}$  in the readout channel with the combination of a mixed-signal feedback loop and correlated double sampling.

Chip total power consumption is about 138mW including 64mW for on-chip electromagnets, 68mW for 16 sensors (the same row in bank I and Q) and 6mW for readout. Total noise is dominated by sensor element ( $97 \text{ nT/Hz}^{1/2}$ ) with readout channel contributing additional  $73 \text{ nT/Hz}^{1/2}$ .

## Chapter 6

# Measurement Results

Bead relaxation and single bead detection are demonstrated with Dynabeads M-450 and M-270 (same magnetic core as M-280). All the Hall-effect sensors are first measured for sensitivity and DC offset. Then single bead relaxation is characterized. Bead detection error is calculated based on signal-to-noise ratio measurement. A magnetic “image” of the microbeads is demonstrated with an 8x8 sensor array. Bead differentiation is performed on three bead samples by comparing their relaxation and complex susceptibility.

## 6.1 Sensor Characterization

The Hall-effect sensors are first characterized without beads to make sure that the bead characterization is unaffected by variations of the sensor elements. The sensitivity of all the sensors is measured with a toroid with air gap and a Gauss meter. The mean voltage-related sensitivity is  $0.029/\text{T}$  (or  $58 \text{ mV/T}$ ) with standard deviation less than 2%. The measured sensitivity is about 35% less than theoretical value calculated from Eq. (4.2). This is likely due to finite-size sense contacts and non-uniform doping profile in the fabricated Hall-effect sensors. This measured sensitivity is used throughout the dissertation for conversion between magnetic field and voltage.

DC offset is measured on 256 sensors from one chip. One-sigma offset is 97 mT and max offset is 210 mT, which is within the 300-mT range designed for the offset servo loop.

## 6.2 Bead Relaxation

Magnetic relaxation of Dynabeads is measured through the following steps. First, before beads are added, responses of all 256 sensors to field modulation or the “baselines” are measured. Next, a 2- $\mu\text{l}$  droplet of diluted Dynabeads (40,000 beads/ $\mu\text{l}$ ) is added to chip surface and dried in air. Responses of all sensors are measured again. Finally beads are washed off and sensors are measured for the third time just for verification purpose.

Magnetic relaxation is observed on those sensors covered with beads. Figure 6-1 shows the normalized post-CDS waveform for one sensor with single M-450 bead and another sensor with single M-270 bead in a separate experiment. Their baseline waveforms are very close so only one baseline is shown here. The beads are magnetized for  $t_m = t_r = 4 \mu\text{s}$ . After switching off  $B_{mag}$  at  $t = 8 \mu\text{s}$ , the sensor response is initially dominated by the readout electronics time constant ( $\sim 16 \text{ ns}$ ), and then by the bead relaxation time constant, which is approximately 370 ns and 300 ns for the M-450 and M-270 beads respectively. After turning off  $B_{mag}$  the bead relaxation signal decreases rapidly and after 250 ns is approximately 40  $\mu\text{T}$  (M-450) and 18  $\mu\text{T}$  (M-270) for beads located near the center of the sensor.

The magnetic relaxation of Dynabeads is observed for modulation frequency ranging from 1 kHz to 1 MHz. This implies the MNPs in Dynabeads are polydisperse.

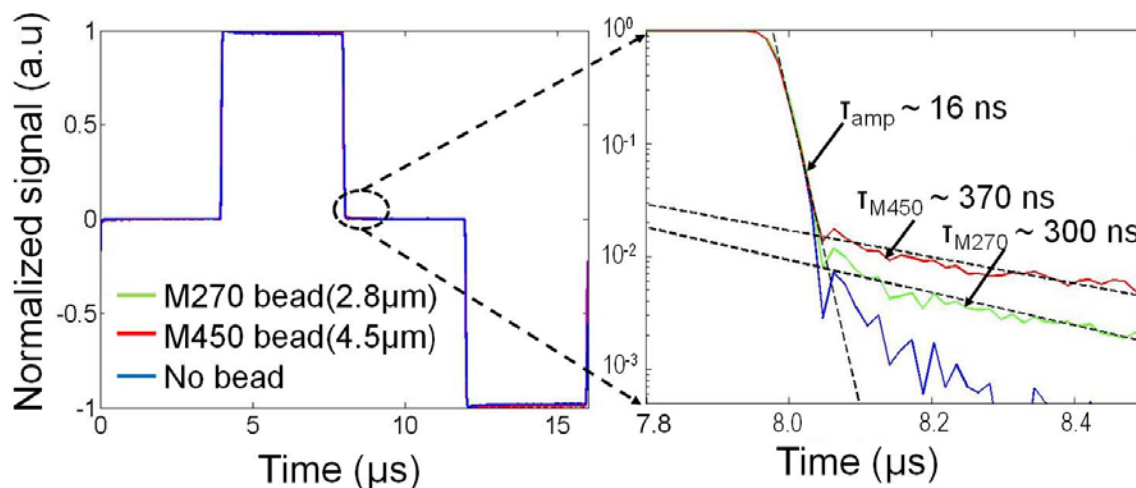


Figure 6-1: Measured Dynabead relaxation signal

To demonstrate the robustness of the magnetic relaxation detection method, baseline variation is measured and compared for both the conventional magnetization detection method and the relaxation method (Figure 6-2). The ambient temperature is changed from 0 to 80 °C. For each detection method, the baseline change is normalized to a 2.8 bead (M-270) signal measured at 30 °C. The relaxation baseline variation is negligible compared to the bead signal whereas the magnetization baseline varies more than a 2.8- $\mu\text{m}$  bead signal when the temperature changes by 3 °C. The temperature coefficient of the magnetization baseline is  $-6.3 \times 10^{-3}/\text{K}$  or  $-19 \mu\text{T}/\text{K}$ , which is dominated by Hall mobility variations and close to experimental values reported by other groups [27]. Note that the Hall-effect sensor is not only susceptible to temperature, but also to other environmental factors such as mechanical stress [27]. Therefore with the magnetization detection method, the baseline must be calibrated carefully to achieve an acceptable detection error. Since this calibration can be performed only when no beads are present near the sensor, it is important that errors remain constant over the course of the measurement. For many biomedical tests incubation of anti-bodies takes several minutes, this requirement is challenging to meet. The proposed detector avoids this issue.

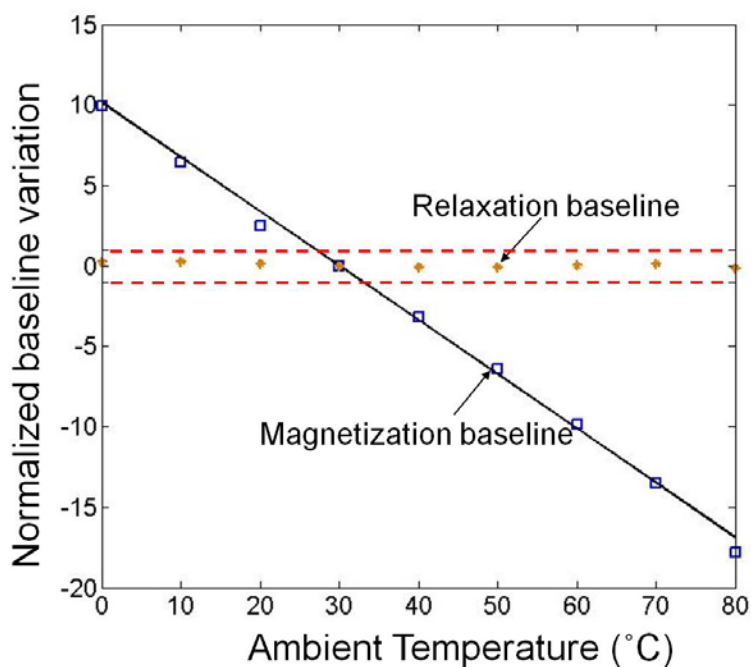


Figure 6-2: Baseline change vs. ambient temperature. The relaxation baseline variation is much smaller than single 2.8- $\mu\text{m}$  bead signal (dotted lines); the magnetization baseline is fitted and its temperature coefficient is 0.33 bead/°C (solid line).

## 6.3 Single Bead Detection

Since the sampling frequency is much higher than the noise bandwidth, the total input-referred noise in each sample can be estimated by  $\sqrt{\frac{v_n^2}{\Delta f} \cdot f_{NBW}}$ , where  $\sqrt{\frac{v_n^2}{\Delta f}}$  is the input-referred noise spectral density which is about 120 nT/Hz<sup>1/2</sup> and  $f_{NBW}$  is noise bandwidth of the readout channel.  $f_{NBW}$  is roughly  $\pi/2$  times the -3dB bandwidth for single-pole RC filter and the approximation is used here for hand calculation. The total noise in each sample is about 475  $\mu$ T, very close to the value given by simulation 440  $\mu$ T.

For the total noise is dominated by thermal noise, then after each CDS, noise power is doubled. Total noise power is inversely dependent on averaging time. The thermal noise model and measured noise are shown in Figure 6-3. Since the flicker noise is suppressed by CDS, the measured noise is dominated by thermal noise up to 10 seconds of averaging time. The measured signal from a M-450 bead and M-270 bead is shown on the same graph. The SNR therefore can be calculated to be 15.9 dB for a 4.5- $\mu$ m bead when the measurement time is 16 ms.

Since the noise is dominated by thermal noise, the probability of detection error for the presence ('1') and absence ('0') of the bead is determined by

$$P_e = \frac{1}{2} \operatorname{erfc} \left( \frac{10^{\frac{SNR}{20}}}{2\sqrt{2}} \right) \quad (6.1)$$

where  $SNR$  is the signal-to-noise ratio in dB. Therefore the probability of detection error is less than 0.1% for 15.9dB SNR. It is important to note that the bead signal used here is for the best case when the bead is near the center of the sensor. When a bead is located between two sensors, SNR drops by 9 dB [33] and the measurement time needs to be increased by eight times to maintain the same probability of detection error.

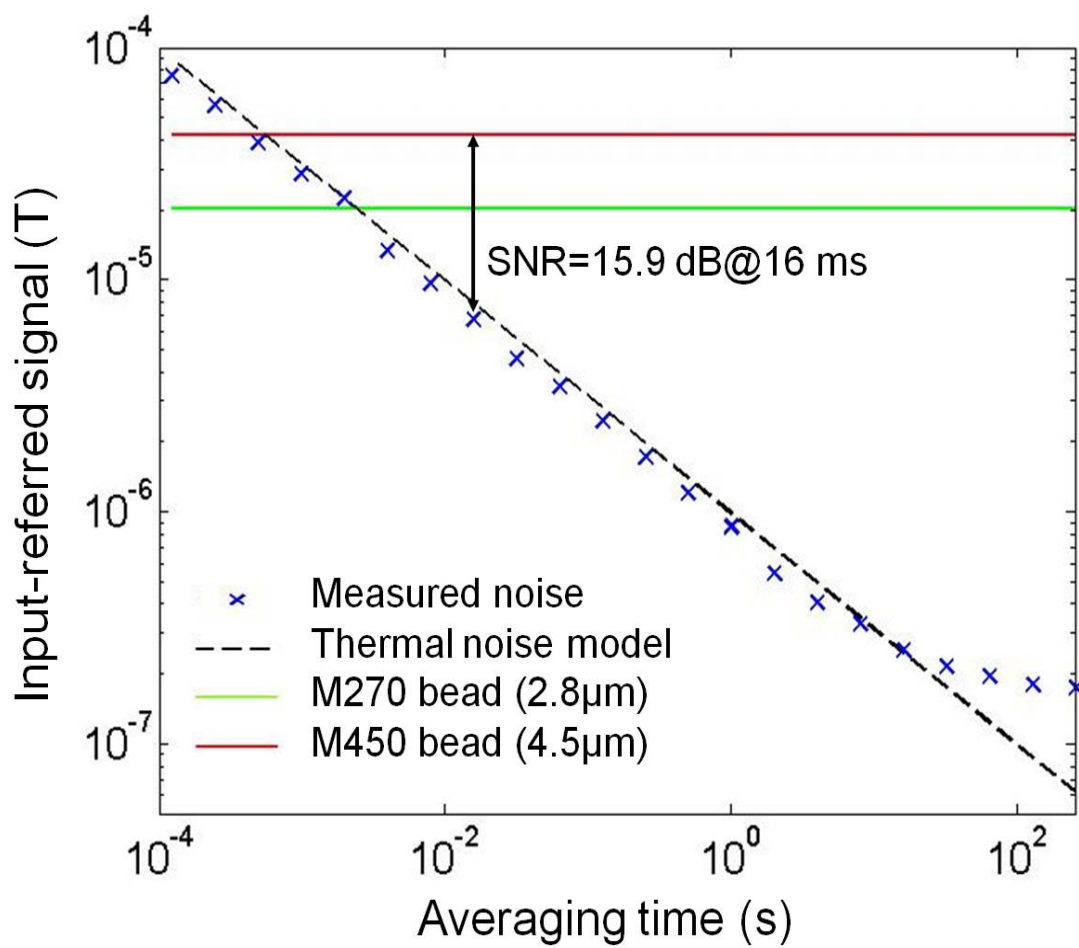


Figure 6-3: Measured signal-to-noise ratio

## 6.4 Bead Imaging

To demonstrate the feasibility of magnetic label detection for biomedical assays, a 2- $\mu\text{l}$  droplet of diluted M-450 bead sample (40,000 beads/ $\mu\text{l}$ ) is added on the chip and air dried. The outputs from a 64-sensor array are shown in Figure 6-4. When the bead sample is dried, the meniscus force drags some beads to the edge of the sensor array window and causes them to clump. Compared to other label detection platforms, this detector adds extra value by monitoring label distribution with micron resolution and providing real-time assay status. The excellent correlation between the optical and the electronic readouts demonstrates the feasibility of robust on-chip detection of magnetic beads using magnetic relaxation.

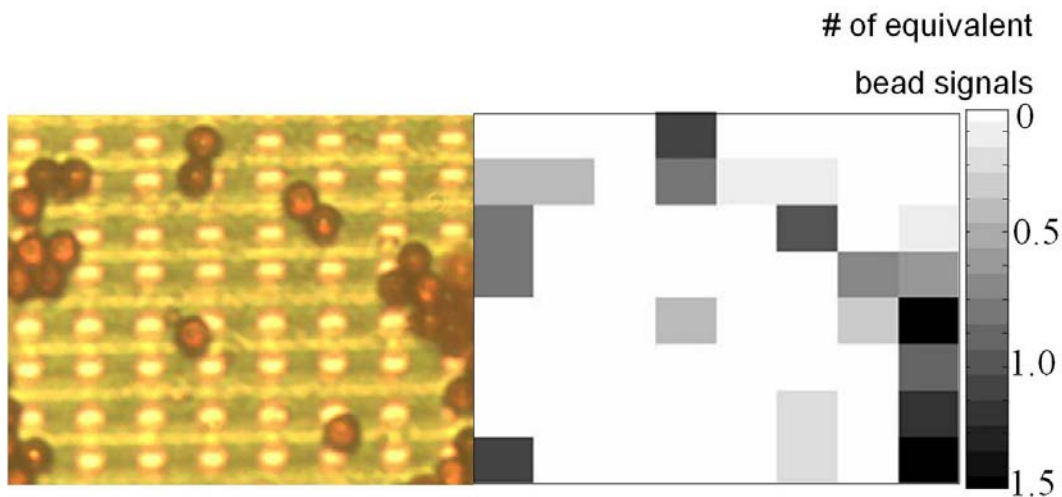


Figure 6-4: Magnetic vs. optical image. Left: sensor array with M-450 beads; right: corresponding electrical signal from the sensors.

## 6.5 Bead Differentiation

The CMOS bead detector has a “dead zone” of only 64 ns, which is more than three orders of magnitude smaller than that achieved on state-of-the-art SQUID [24] and flux-gate [17] sensors and thus it enables relaxation of a wider range of MNPs to be observed. Differentiation of beads is achieved based on their relaxation characteristics.

Three magnetite MNP samples are tested. The first two samples are 20-nm and 25-nm diameter magnetite nanocrystals with oleic acid coating (catalog number SOR-20-50 and SOR-25-50, Ocean NanoTech, Springdale, Arkansas, USA). The third sample contains 1- $\mu\text{m}$  magnetic beads suspended in double-distilled water at a concentration of 50 mg [solids]/ml with 22.5 mg [Fe]/ml (SiMAG/K-Silanol, Chemicell GmbH, Berlin, Germany). The SiMAG bead consists of multiple magnetite nanoparticle cores embedded in a silica matrix.

Since the total sensor area is only 68  $\mu\text{m}$  x 48  $\mu\text{m}$ , samples of sub- $\mu\text{l}$  volume contain enough MNPs to cover the sensor surfaces. In our experiments, a sample of each MNP is diluted and air dried on one sensor chip. The sensor chips are calibrated before the MNPs are immobilized on the sensor surface. To increase the signal-to-noise ratio (SNR), each measurement is averaged for 8 seconds. Data is then averaged over multiple sensors to further reduce measurement variation.

The relaxation curves after CDS are shown in Figure 6-5. For  $t_m = t_r = 1 \mu\text{s}$ , there is no visible relaxation from the SOR-20-50 sample whereas for the SOR-25-50 and SiMAG, relaxation is observed and can be clearly distinguished (Figure 6-5a). There are two possible causes that no relaxation is detected on the SOR-20-50 MNPs. First, the MNPs could have fairly large energy barrier so there is not enough time to magnetize them during  $t_m$ ; second, the MNPs could have such a small anisotropy energy that they relax very fast and cannot be detected. The first cause is unlikely because no relaxation is observed for the SOR-20-50 MNPs even when the magnetization time is increased to 4  $\mu\text{s}$ , 16  $\mu\text{s}$  and 64  $\mu\text{s}$  (Fig. 4b-d). This implies that the Néel relaxation time of SOR-20-50 is far less than the 64 ns “dead zone”.

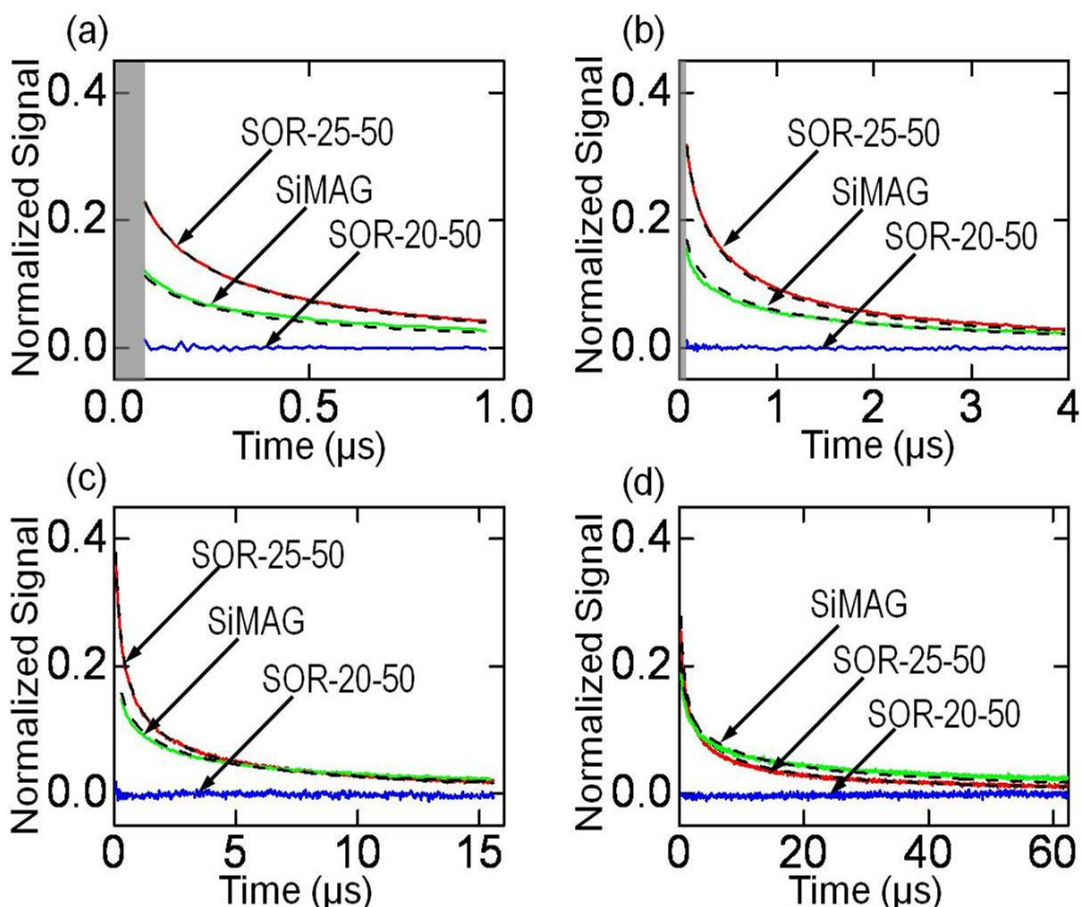


Figure 6-5: Measured relaxation curves (solid lines) and model (dotted). The “dead zone” is shaded. (a)  $t_m = t_r = 1 \mu\text{s}$ ; (b)  $t_m = t_r = 4 \mu\text{s}$ ; (c)  $t_m = t_r = 16 \mu\text{s}$ ; (d)  $t_m = t_r = 64 \mu\text{s}$ .

To verify this hypothesis, complex susceptibility is measured on Quantum Design MPMS-XL SQUID magnetometer (San Diego, CA) (Figure 6-6). For SOR-20-50, both real and imaginary part of the complex susceptibility is quite flat through the frequencies. This shows the signal from most MNPs in SOR-20-50 decays very fast and is out of the detection range of the SQUID magnetometer. SOR-20-50 is also tested for DC magnetization and shows superparamagnetic property. The complex susceptibility measurement, together with the relaxation measurement discussed in previous paragraph, proves that relaxation from SOR-20-50 decays with time constants much less than the 64-ns “dead zone”.

Both the SOR-25-50 MNPs and SiMAG beads show relaxation. However, their relaxation curves differ, which indicates that their internal magnetic properties such as anisotropy energy and volume distribution are different. Based on the moment superposition model proposed in [18] and assuming that the MNP volume distribution in each sample follows a log-normal function, our analysis [23] shows that the SOR-25-50 MNPs have a bigger portion of MNPs with anisotropy energy larger than  $1 kT$  and narrower distribution of MNP size than the SiMAG beads.

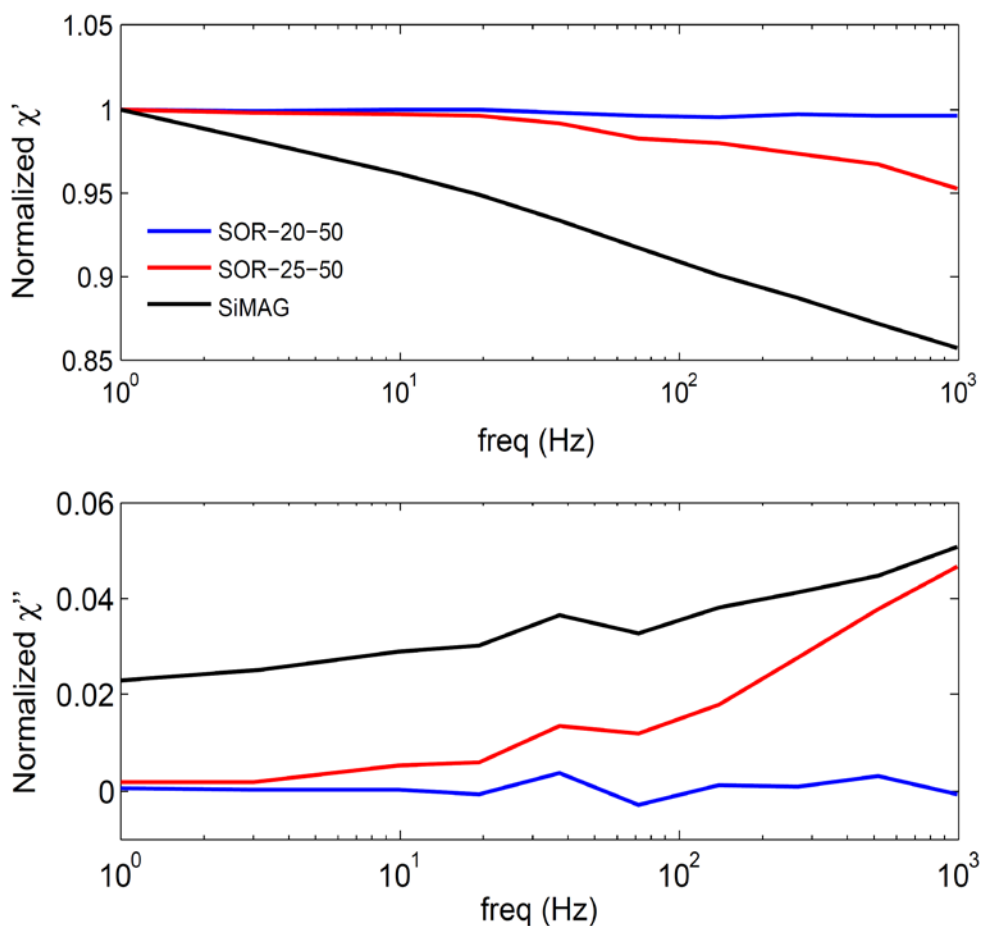


Figure 6-6: Real (top) and imaginary part (bottom) of the measured complex susceptibility on the three MNP samples: 20-nm MNP (blue), 25-nm MNP (red) and SiMAG (black). The values are normalized to DC susceptibility.

## 6.6 Summary

Dynabeads with relaxation time constants of several hundred nanoseconds are measured. Single M-450 bead is detected in 16 ms with a probability of detection error less than 0.1%. An 8x8 sensor array captures magnetic images of the beads located on its surface with micron resolution with high correlation to the optical image of the beads.

Differentiation of three commercially-available MNP samples by their relaxation and complex susceptibility is demonstrated. Compared to prior instruments exploiting MRX, the CMOS solution might have the potential of measuring very fast magnetic relaxation with time constant as small as 64 ns. This could allow a wide selection of MNPs to be used as labels in magnetic immunoassays.

The performance of the microbead label detector is summarized in Table 6-1.

Table 6-1: Chip Performance Summary

<b>Technology</b>	0.18 $\mu\text{m}$ CMOS 2P6M
<b>Area</b>	2.5x2.5 $\text{mm}^2$ (Chip)
	8.5x6 $\mu\text{m}^2$ (Sensor element)
<b>Power</b>	64 mW (Electromagnet)
	4.2 mW (Sensor element)
	6.2 mW (PGA+DAC)
<b>Sensitivity</b>	0.029/T (Sensor element)
<b>Input-referred noise</b>	97 nT/Hz <sup>1/2</sup> (Sensor element)
	73 nT/Hz <sup>1/2</sup> (PGA+DAC)
<b>Readout channel bandwidth</b>	10 MHz
<b>Input-referred offset</b>	< 1 $\mu\text{T}$
<b>Probability of detection error</b>	0.1% in 16 ms for 4.5 $\mu\text{m}$ bead

## Chapter 7

# Conclusions and Future Work

### 7.1 Conclusions

A CMOS chip for evaluating biomedical assays labeled with magnetic microbeads is presented. The label detection is based on measuring the magnetic relaxation signature from beads. Compared to conventional magnetization-based detection method, the relaxation approach significantly reduces sensitivity to environmental variations such as temperature and eliminates the need for individual sensor's baseline calibration or any reference sensors.

On-chip current loops are used to magnetize the beads, thus eliminating the need for an external magnet. This reduces overall system power dissipation from Watts to milli-Watts, meeting the requirements of portable applications. The Hall-effect sensors used are compatible with standard CMOS technology, greatly reducing cost compared to other solutions that require specialized processes.

Relaxation-based magnetic bead detection, imaging and differentiation are demonstrated on a CMOS chip for the first time. Robust, compact, low-power and low-cost magnetic bead detection based on magnetic relaxation is suitable for point-of-care biomedical applications.

## 7.2 Future Work

The CMOS bead detector presented in this dissertation is proven to be a compact and robust solution for point-of-care applications. A chip with a larger sensor array and parallel readout channels [35], integrated with a microfluidic system [36], enables larger label detection area and faster detection time for high-sensitivity bioassays. Since unbound MNP labels in suspension are also subject to Brownian relaxation, by choosing MNPs of suitable sizes, MNPs bound to the targets can be distinguished from unbound MNPs without any washing step [10].

The scalability of Hall-effect sensors will drive the magnetic imaging resolution to sub-micron and potentially could lead to applications such as molecular level sensing. The differentiation of MNPs through relaxation is expected to make “multi-color” magnetic labels available and could potentially challenge the dominance of optical sensors and fluorescent labels in the near future.

## Bibliography

- [1] M. Urdea, *et al.*, "Requirements for high impact diagnostics in the developing world," *Nature*, vol. 444 Suppl 1, pp. 73-79, Nov 23 2006.
- [2] F. B. Myers and L. P. Lee, "Innovations in optical microfluidic technologies for point-of-care diagnostics," *Lab Chip*, vol. 8, pp. 2015-2031, Dec 2008.
- [3] C. B. Kriz, K. Radevik, and D. Kriz, "Magnetic permeability measurements in bioanalysis and biosensors," *Anal Chem*, vol. 68, pp. 1966-1970, Jun 1 1996.
- [4] R. Kotitz, *et al.*, "SQUID based remanence measurements for immunoassays," *Applied Superconductivity, IEEE Transactions on*, vol. 7, pp. 3678-3681, 1997.
- [5] D. R. Baselt, *et al.*, "A biosensor based on magnetoresistance technology," *Biosens Bioelectron*, vol. 13, pp. 731-739, Oct 1 1998.
- [6] O. Florescu, *et al.*, "On-chip magnetic separation of superparamagnetic beads for integrated molecular analysis," *J Appl Phys*, vol. 107, p. 54702, Mar 1 2010.
- [7] K. M. Krishnan, "Biomedical Nanomagnetism: A Spin Through Possibilities in Imaging, Diagnostics, and Therapy," *IEEE Trans Magn*, vol. 46, pp. 2523-2558, Jul 1 2010.
- [8] G. Fønnum, C. Johansson, A. Molteberg, S. Mørup, and E. Aksnes, "Characterisation of Dynabeads® by magnetization measurements and Mössbauer spectroscopy," *Journal of Magnetism and Magnetic Materials*, vol. 293, pp. 41-47, 2005.
- [9] P.-A. Besse, G. Boero, M. Demierre, V. Pott, and R. Popovic, "Detection of a single magnetic microbead using a miniaturized silicon Hall sensor," *Applied Physics Letters*, vol. 80, pp. 4199-4201, 2002.
- [10] Y. R. Chemla, *et al.*, "Ultrasensitive magnetic biosensor for homogeneous immunoassay," *Proc Natl Acad Sci U S A*, vol. 97, pp. 14268-14272, Dec 19 2000.
- [11] D. L. Graham, H. A. Ferreira, P. P. Freitas, and J. M. Cabral, "High sensitivity detection of molecular recognition using magnetically labelled biomolecules and magnetoresistive sensors," *Biosens Bioelectron*, vol. 18, pp. 483-488, Apr 2003.
- [12] G. Li, *et al.*, "Spin valve sensors for ultrasensitive detection of superparamagnetic nanoparticles for biological applications," *Sens Actuators A Phys*, vol. 126, pp. 98-106, 2006.

- [13] T. Aytur, *et al.*, "A novel magnetic bead bioassay platform using a microchip-based sensor for infectious disease diagnosis," *J Immunol Methods*, vol. 314, pp. 21-29, Jul 31 2006.
- [14] O. Florescu, M. Mattmann, and B. Boser, "Fully integrated detection of single magnetic beads in complementary metal-oxide-semiconductor," *Journal of Applied Physics*, vol. 103, p. 046101, 2008.
- [15] H. Wang, Y. Chen, A. Hassibi, A. Scherer, and A. Hajimiri, "A frequency-shift CMOS magnetic biosensor array with single-bead sensitivity and no external magnet," in *Solid-State Circuits Conference - Digest of Technical Papers, 2009. ISSCC 2009. IEEE International*, 2009, pp. 438-439,439a.
- [16] K. Enpuku, *et al.*, "Magnetic immunoassays utilizing magnetic markers and a high-Tc SQUID," *Applied Superconductivity, IEEE Transactions on*, vol. 15, pp. 660-663, 2005.
- [17] F. Ludwig, E. Heim, and M. Schilling, "Characterization of superparamagnetic nanoparticles by analyzing the magnetization and relaxation dynamics using fluxgate magnetometers," *Journal of Applied Physics*, vol. 101, p. 113909, 2007.
- [18] R. W. Chantrell, S. R. Hoon, and B. K. Tanner, "Time-dependent magnetization in fine-particle ferromagnetic systems," *Journal of Magnetism and Magnetic Materials*, vol. 38, pp. 133-141, 1983.
- [19] P. C. Fannin and S. W. Charles, "On the calculation of the Neel relaxation time in uniaxial single-domain ferromagnetic particles," *Journal of Physics D: Applied Physics*, vol. 27, p. 185, 1994.
- [20] W. F. Brown, Jr., "Thermal Fluctuations of a Single-Domain Particle," *Physical Review*, vol. 130, pp. 1677-1686, 1963.
- [21] L. Bessais, L. Ben Jaffel, and J. L. Dormann, "Relaxation time of fine magnetic particles in uniaxial symmetry," *Physical Review B*, vol. 45, pp. 7805-7815, 1992.
- [22] A. Aharoni, "Susceptibility resonance and magnetic viscosity," *Physical Review B*, vol. 46, pp. 5434-5441, 1992.
- [23] P. Liu, K. Skucha, M. Megens, and B. Boser, "A CMOS Hall-Effect Sensor for the Characterization and Detection of Magnetic Nanoparticles for Biomedical Applications," *Magnetics, IEEE Transactions on*, vol. 47, pp. 3449-3451, 2011.
- [24] N. L. Adolphi, *et al.*, "Characterization of magnetite nanoparticles for SQUID-relaxometry and magnetic needle biopsy," *J Magn Magn Mater*, vol. 321, pp. 1459-1464, May 1 2009.
- [25] D. Eberbeck, F. Wiekhorst, U. Steinhoff, and L. Trahms, "Aggregation behaviour of magnetic nanoparticle suspensions investigated by magnetorelaxometry," *Journal of Physics: Condensed Matter*, vol. 18, p. S2829, 2006.
- [26] P. C. Fannin, *et al.*, "Investigation of the complex susceptibility of magnetic beads containing maghemite nanoparticles," *Journal of Magnetism and Magnetic Materials*, vol. 303, pp. 147-152, 2006.

- [27] R. S. Popovic, *Hall effect devices : magnetic sensors and characterization of semiconductors*. Bristol, England ; Philadelphia: A. Hilger, 1991.
- [28] O. Florescu, *et al.*, "On-chip magnetic separation of superparamagnetic beads for integrated molecular analysis," *Journal of Applied Physics*, vol. 107, p. 054702, 2010.
- [29] T. H. Geballe and G. W. Hull, "Seebeck Effect in Silicon," *Physical Review*, vol. 98, pp. 940-947, 1955.
- [30] C. C. Enz and G. C. Temes, "Circuit techniques for reducing the effects of op-amp imperfections: autozeroing, correlated double sampling, and chopper stabilization," *Proceedings of the IEEE*, vol. 84, pp. 1584-1614, 1996.
- [31] A. Hassibi, S. Zahedi, R. Navid, R. W. Dutton, and T. H. Lee, "Biological shot-noise and quantum-limited signal-to-noise ratio in affinity-based biosensors," *Journal of Applied Physics*, vol. 97, pp. 084701-084701-084710, 2005.
- [32] P. P. Liu, *et al.*, "Magnetic Relaxation Detector for Microbead Labels," *Solid-State Circuits, IEEE Journal of*, vol. 47, pp. 1056-1064, 2012.
- [33] K. Skucha, P. Liu, M. Megens, J. Kim, and B. Boser, "A compact Hall-effect sensor array for the detection and imaging of single magnetic beads in biomedical assays," in *Solid-State Sensors, Actuators and Microsystems Conference (TRANSDUCERS), 2011 16th International*, 2011, pp. 1833-1836.
- [34] K. Ishibashi, K. Takasugi, T. Hashimoto, and K. Sasaki, "A 1-V TFT-load SRAM using a two-step word-voltage method," *Solid-State Circuits, IEEE Journal of*, vol. 27, pp. 1519-1524, 1992.
- [35] S. Gambini, *et al.*, "A CMOS 10kpixel baseline-free magnetic bead detector with column-parallel readout for miniaturized immunoassays," in *Solid-State Circuits Conference Digest of Technical Papers (ISSCC), 2012 IEEE International*, 2012, pp. 126-128.
- [36] A. Wu, L. Wang, E. Jensen, R. Mathies, and B. Boser, "Modular integration of electronics and microfluidic systems using flexible printed circuit boards," *Lab on a Chip*, vol. 10, pp. 519-521, 2010.